Application of lattice Boltzmann methods for wind turbine wake simulation

Ralf Deiterding

Aerodynamics and Flight Mechanics Research Group
Department of Aeronautics & Astronautics
University of Southampton
Boldrewood Campus, Southampton SO16 7QF, UK
E-mail: r.deiterding@soton.ac.uk

February 26, 2021

Outline

Collaboration with / Results from

- Mikael Grondeau on grant *Aerodynamics and aeroacoustics of turbulent flows over and past permeable rough surfaces* (EPSRC - EP/S013296/1)
- Stephen Wood (now NASA) – *Lattice Boltzmann methods for wind energy analysis*, PhD thesis, University Tennessee Knoxville, Aug 2016.
- Christos Gkoudesnes – *Implementation and verification of LES models for SRT lattice Boltzmann methods*, PhD thesis, University of Southampton, defense Mar 2021.
- Aden Cox – *Actuator line modelling of wind turbines*, undergraduate individual project, University of Southampton, May 2017.
- Antonio Reyes Barraza – *Lattice Boltzmann method on hybrid boundary layer and Cartesian adaptive mesh refinement*, PhD thesis, University of Southampton, defense end of 2021.

Approximation of Boltzmann equation

Is based on solving the Boltzmann equation with a simplified collision operator

$$\partial_t f + \mathbf{u} \cdot \nabla f = \omega(f^{eq} - f) + F$$

- $\mathrm{Kn} = l_f/L \ll 1$, where l_f is replaced with Δx
- Weak compressibilty and small Mach number assumed

Approximation of Boltzmann equation

Is based on solving the Boltzmann equation with a simplified collision operator

$$\partial_t f + \mathbf{u} \cdot \nabla f = \omega(f^{eq} - f) + F$$

- $\mathrm{Kn} = l_f / L \ll 1$, where l_f is replaced with Δx
- Weak compressibilty and small Mach number assumed

Equation is approximated in simplified phase space and with a splitting approach.

1.) Transport step solves $\partial_t f_\alpha + \mathbf{e}_\alpha \cdot \nabla f_\alpha = 0$

Operator: $\mathcal{T}$: $\tilde{f}_\alpha(\mathbf{x} + \mathbf{e}_\alpha \Delta t, t + \Delta t) = f_\alpha(\mathbf{x}, t)$

$$\rho(\mathbf{x}, t) = \sum_{\alpha=0}^{18} f_\alpha(\mathbf{x}, t), \quad \rho(\mathbf{x}, t) u_i(\mathbf{x}, t) = \sum_{\alpha=0}^{18} \mathbf{e}_{\alpha i} f_\alpha(\mathbf{x}, t)$$

Approximation of Boltzmann equation

Is based on solving the Boltzmann equation with a simplified collision operator

$$\partial_t f + \mathbf{u} \cdot \nabla f = \omega(f^{eq} - f) + F$$

- $\mathrm{Kn} = l_f / L \ll 1$, where l_f is replaced with Δx
- Weak compressibilty and small Mach number assumed

Equation is approximated in simplified phase space and with a splitting approach.

1.) Transport step solves $\partial_t f_\alpha + \mathbf{e}_\alpha \cdot \nabla f_\alpha = 0$

Operator: $\mathcal{T}$: $\tilde{f}_\alpha(\mathbf{x} + \mathbf{e}_\alpha \Delta t, t + \Delta t) = f_\alpha(\mathbf{x}, t)$

$$\rho(\mathbf{x}, t) = \sum_{\alpha=0}^{18} f_\alpha(\mathbf{x}, t), \quad \rho(\mathbf{x}, t) u_i(\mathbf{x}, t) = \sum_{\alpha=0}^{18} \mathbf{e}_{\alpha i} f_\alpha(\mathbf{x}, t)$$

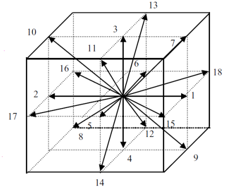

Discrete velocities:

$$\mathbf{e}_\alpha = \begin{cases} 0, & \alpha = 0, \\ (\pm 1, 0, 0)c, (0, \pm 1, 0)c, (0, 0, \pm 1)c, & \alpha = 1, \dots, 6, \\ (\pm 1, \pm 1, 0)c, (\pm 1, 0, \pm 1)c, (0, \pm 1, \pm 1)c, & \alpha = 7, \dots, 18 \end{cases}$$

$c = \dfrac{\Delta x}{\Delta t}$, Physical speed of sound: $c_s = \dfrac{c}{\sqrt{3}}$

Approximation of thermal equilibrium

2.) Collision step solves $\partial_t f_\alpha = \omega(f_\alpha^{eq} - f_\alpha) + F_\alpha$
Operator $\mathcal{C}$:

$$f_\alpha(\cdot, t+\Delta t) = \tilde{f}_\alpha(\cdot, t+\Delta t) + \omega_L \Delta t \left(\tilde{f}_\alpha^{eq}(\cdot, t+\Delta t) - \tilde{f}_\alpha(\cdot, t+\Delta t)\right) + \Delta t F_\alpha$$

with $F_\alpha = 3\rho t_\alpha \mathbf{e}_\alpha \mathbf{F}/c^2$ and equilibrium function

$$f_\alpha^{eq}(\rho, \mathbf{u}) = \rho t_\alpha \left[1 + \frac{3\mathbf{e}_\alpha \mathbf{u}}{c^2} + \frac{9(\mathbf{e}_\alpha \mathbf{u})^2}{2c^4} - \frac{3\mathbf{u}^2}{2c^2} + \qquad \right]$$

with $t_\alpha = \frac{1}{9}\left\{3, \frac{1}{2}, \frac{1}{2}, \frac{1}{2}, \frac{1}{2}, \frac{1}{2}, \frac{1}{2}, \frac{1}{4}, \frac{1}{4}, \frac{1}{4}, \frac{1}{4}, \frac{1}{4}, \frac{1}{4}, \frac{1}{4}, \frac{1}{4}, \frac{1}{4}, \frac{1}{4}, \frac{1}{4}, \frac{1}{4},\right\}$
Pressure $\delta p = \sum_\alpha f_\alpha^{eq} c_s^2 = \rho c_s^2$.
Dev. stress $\Sigma_{ij} = \left(1 - \frac{\omega_L \Delta t}{2}\right) \sum_\alpha \mathbf{e}_{\alpha i} \mathbf{e}_{\alpha j} (f_\alpha^{eq} - f_\alpha)$

Approximation of thermal equilibrium

2.) Collision step solves $\partial_t f_\alpha = \omega(f_\alpha^{eq} - f_\alpha) + F_\alpha$
Operator $\mathcal{C}$:

$$f_\alpha(\cdot, t+\Delta t) = \tilde{f}_\alpha(\cdot, t+\Delta t) + \omega_L \Delta t \left(\tilde{f}_\alpha^{eq}(\cdot, t+\Delta t) - \tilde{f}_\alpha(\cdot, t+\Delta t) \right) + \Delta t F_\alpha$$

with $F_\alpha = 3\rho t_\alpha \mathbf{e}_\alpha \mathbf{F}/c^2$ and equilibrium function

$$f_\alpha^{eq}(\rho, \mathbf{u}) = \rho t_\alpha \left[1 + \frac{3\mathbf{e}_\alpha \mathbf{u}}{c^2} + \frac{9(\mathbf{e}_\alpha \mathbf{u})^2}{2c^4} - \frac{3\mathbf{u}^2}{2c^2} + \frac{\mathbf{e}_\alpha \mathbf{u}}{3c^2} \left(\frac{9(\mathbf{e}_\alpha \mathbf{u})^2}{2c^4} - \frac{3\mathbf{u}^2}{2c^2} \right) \right]$$

with $t_\alpha = \frac{1}{9}\left\{3, \frac{1}{2}, \frac{1}{2}, \frac{1}{2}, \frac{1}{2}, \frac{1}{2}, \frac{1}{2}, \frac{1}{4}, \frac{1}{4}, \frac{1}{4}, \frac{1}{4}, \frac{1}{4}, \frac{1}{4}, \frac{1}{4}, \frac{1}{4}, \frac{1}{4}, \frac{1}{4}, \frac{1}{4}, \frac{1}{4}, \right\}$
Pressure $\delta p = \sum_\alpha f_\alpha^{eq} c_s^2 = \rho c_s^2$.
Dev. stress $\Sigma_{ij} = \left(1 - \frac{\omega_L \Delta t}{2}\right) \sum_\alpha \mathbf{e}_{\alpha i} \mathbf{e}_{\alpha j} (f_\alpha^{eq} - f_\alpha)$

Approximation of thermal equilibrium

2.) Collision step solves $\partial_t f_\alpha = \omega(f_\alpha^{eq} - f_\alpha) + F_\alpha$
Operator $\mathcal{C}$:

$$f_\alpha(\cdot, t+\Delta t) = \tilde{f}_\alpha(\cdot, t+\Delta t) + \omega_L \Delta t \left(\tilde{f}_\alpha^{eq}(\cdot, t+\Delta t) - \tilde{f}_\alpha(\cdot, t+\Delta t) \right) + \Delta t F_\alpha$$

with $F_\alpha = 3\rho t_\alpha \mathbf{e}_\alpha \mathbf{F}/c^2$ and equilibrium function

$$f_\alpha^{eq}(\rho, \mathbf{u}) = \rho t_\alpha \left[1 + \frac{3\mathbf{e}_\alpha \mathbf{u}}{c^2} + \frac{9(\mathbf{e}_\alpha \mathbf{u})^2}{2c^4} - \frac{3\mathbf{u}^2}{2c^2} + \frac{\mathbf{e}_\alpha \mathbf{u}}{3c^2} \left(\frac{9(\mathbf{e}_\alpha \mathbf{u})^2}{2c^4} - \frac{3\mathbf{u}^2}{2c^2} \right) \right]$$

with $t_\alpha = \frac{1}{9}\left\{3, \frac{1}{2}, \frac{1}{2}, \frac{1}{2}, \frac{1}{2}, \frac{1}{2}, \frac{1}{2}, \frac{1}{4}, \frac{1}{4}, \frac{1}{4}, \frac{1}{4}, \frac{1}{4}, \frac{1}{4}, \frac{1}{4}, \frac{1}{4}, \frac{1}{4}, \frac{1}{4}, \frac{1}{4}, \frac{1}{4}, \right\}$
Pressure $\delta p = \sum_\alpha f_\alpha^{eq} c_s^2 = \rho c_s^2$.
Dev. stress $\Sigma_{ij} = \left(1 - \frac{\omega_L \Delta t}{2}\right) \sum_\alpha \mathbf{e}_{\alpha i} \mathbf{e}_{\alpha j} (f_\alpha^{eq} - f_\alpha)$
A Chapman-Enskog expansion ($f_\alpha = f_\alpha(0) + \epsilon f_\alpha(1) + \epsilon^2 f_\alpha(2) + \ldots$) shows that

$$\partial_t \rho + \nabla \cdot (\rho \mathbf{u}) = 0, \qquad \partial_t \mathbf{u} + \mathbf{u} \cdot \nabla \mathbf{u} = -\nabla p + \nu \nabla^2 \mathbf{u} + \mathbf{F}$$

are recoverd to $O(\epsilon^{2,3})$ [Hou et al., 1996] and also $\omega_L = \tau_L^{-1} = \dfrac{c_s^2}{\nu + \Delta t c_s^2/2}$

Level-set method for boundary embedding

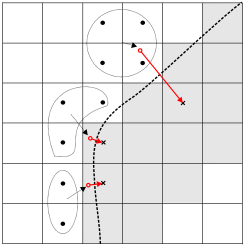

- Implicit boundary representation via distance function φ, normal $\mathbf{n} = \nabla\varphi / |\nabla\varphi|$.
- Construction of macro-values in embedded boundary cells by interpolation / extrapolation.
- Complex boundary moving with local velocity $\mathbf{w}$, ghost cell velocity: $\mathbf{u}' = 2\mathbf{w} - \mathbf{u}$

Level-set method for boundary embedding

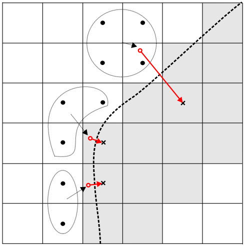

- Implicit boundary representation via distance function φ, normal $\mathbf{n} = \nabla\varphi / |\nabla\varphi|$.
- Construction of macro-values in embedded boundary cells by interpolation / extrapolation.
- Complex boundary moving with local velocity $\mathbf{w}$, ghost cell velocity: $\mathbf{u}' = 2\mathbf{w} - \mathbf{u}$
- Then use $f_\alpha^{eq}(\rho', \mathbf{u}')$ to construct distributions in embedded ghost cells.
- Wall function acts on first layer of exterior cells. Sets shear velocity according to Spalding function.
- Distance computation for triangulated grids with CPT algorithm [Mauch, 2000].

Level-set method for boundary embedding

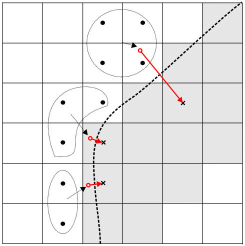

- Implicit boundary representation via distance function φ, normal $\mathbf{n} = \nabla\varphi / |\nabla\varphi|$.
- Construction of macro-values in embedded boundary cells by interpolation / extrapolation.
- Complex boundary moving with local velocity $\mathbf{w}$, ghost cell velocity: $\mathbf{u}' = 2\mathbf{w} - \mathbf{u}$
- Then use $f_\alpha^{eq}(\rho', \mathbf{u}')$ to construct distributions in embedded ghost cells.
- Wall function acts on first layer of exterior cells. Sets shear velocity according to Spalding function.
- Distance computation for triangulated grids with CPT algorithm [Mauch, 2000].

Block-structured adaptive mesh refinement (SAMR)

- Refinement in all spatial directions and time by same factor
- Refined blocks overlay coarser ones
- Most efficient LBM implementation with patch-wise for-loops
- LBM implemented on finite volume grids
- AMROC V3.0 with significantly enhanced parallelization [Deiterding et al., 2007, Deiterding, 2011, Deiterding and Wood, 2015, Deiterding et al., 2006]

Turbulence modeling

Pursue a large-eddy simulation approach with $\overline{f}_\alpha$ and $\overline{f}_\alpha^{eq}$, i.e.

1.) $\tilde{\overline{f}}_\alpha(\mathbf{x} + \mathbf{e}_\alpha \Delta t, t + \Delta t) = \overline{f}_\alpha(\mathbf{x}, t)$

2.) $\overline{f}_\alpha(\cdot, t + \Delta t) = \tilde{\overline{f}}_\alpha(\cdot, t + \Delta t) + \frac{1}{\tau^\star} \Delta t \left(\tilde{\overline{f}}_\alpha^{eq}(\cdot, t + \Delta t) - \tilde{\overline{f}}_\alpha(\cdot, t + \Delta t) \right)$

Turbulence modeling

Pursue a large-eddy simulation approach with $\bar{f}_\alpha$ and $\bar{f}^{eq}_\alpha$, i.e.

1.) $\tilde{\bar{f}}_\alpha(\mathbf{x}+\mathbf{e}_\alpha\Delta t, t+\Delta t) = \bar{f}_\alpha(\mathbf{x}, t)$

2.) $\bar{f}_\alpha(\cdot, t+\Delta t) = \tilde{\bar{f}}_\alpha(\cdot, t+\Delta t) + \frac{1}{\tau^\star}\Delta t \left(\tilde{\bar{f}}^{eq}_\alpha(\cdot, t+\Delta t) - \tilde{\bar{f}}_\alpha(\cdot, t+\Delta t)\right)$

Effective viscosity: $\nu^\star = \nu + \nu_t = \dfrac{1}{3}\left(\dfrac{\tau_L^\star}{\Delta t} - \dfrac{1}{2}\right) c\Delta x \quad \text{with} \quad \tau_L^\star = \tau_L + \tau_t$

Turbulence modeling

Pursue a large-eddy simulation approach with $\bar{f}_\alpha$ and $\bar{f}^{eq}_\alpha$, i.e.

1.) $\tilde{\bar{f}}_\alpha(\mathbf{x}+\mathbf{e}_\alpha \Delta t, t+\Delta t) = \bar{f}_\alpha(\mathbf{x},t)$

2.) $\bar{f}_\alpha(\cdot, t+\Delta t) = \tilde{\bar{f}}_\alpha(\cdot, t+\Delta t) + \frac{1}{\tau^\star}\Delta t \left(\tilde{\bar{f}}^{eq}_\alpha(\cdot, t+\Delta t) - \tilde{\bar{f}}_\alpha(\cdot, t+\Delta t)\right)$

Effective viscosity: $\nu^\star = \nu + \nu_t = \dfrac{1}{3}\left(\dfrac{\tau_L^\star}{\Delta t} - \dfrac{1}{2}\right) c\Delta x \quad \text{with} \quad \tau_L^\star = \tau_L + \tau_t$

Use Smagorinsky model to evaluate ν_t, e.g., $\nu_t = (C_{sm}\Delta x)^2 |\bar{\mathbf{S}}|$, where

$$|\bar{\mathbf{S}}| = \sqrt{2\sum_{i,j} \bar{S}_{ij}\bar{S}_{ij}}$$

The filtered strain rate tensor $\bar{S}_{ij} = (\partial_j \bar{u}_i + \partial_i \bar{u}_j)/2$ can be computed as a second moment as

$$\bar{S}_{ij} = \frac{\bar{\Sigma}_{ij}}{2\rho c_s^2 \tau_L^\star \left(1 - \frac{\omega_L \Delta t}{2}\right)} = \frac{1}{2\rho c_s^2 \tau_L^\star} \sum_\alpha e_{\alpha i} e_{\alpha j} (\bar{f}^{eq}_\alpha - \bar{f}_\alpha)$$

Turbulence modeling

Pursue a large-eddy simulation approach with $\bar{f}_\alpha$ and $\bar{f}^{eq}_\alpha$, i.e.

1.) $\tilde{\bar{f}}_\alpha(\mathbf{x}+\mathbf{e}_\alpha\Delta t, t+\Delta t) = \bar{f}_\alpha(\mathbf{x}, t)$

2.) $\bar{f}_\alpha(\cdot, t+\Delta t) = \tilde{\bar{f}}_\alpha(\cdot, t+\Delta t) + \frac{1}{\tau^\star}\Delta t \left(\tilde{\bar{f}}^{eq}_\alpha(\cdot, t+\Delta t) - \tilde{\bar{f}}_\alpha(\cdot, t+\Delta t)\right)$

Effective viscosity: $\nu^\star = \nu + \nu_t = \dfrac{1}{3}\left(\dfrac{\tau_L^\star}{\Delta t} - \dfrac{1}{2}\right) c\Delta x \quad \text{with} \quad \tau_L^\star = \tau_L + \tau_t$

Use Smagorinsky model to evaluate ν_t, e.g., $\nu_t = (C_{sm}\Delta x)^2|\bar{\mathbf{S}}|$, where

$$|\bar{\mathbf{S}}| = \sqrt{2\sum_{i,j}\bar{S}_{ij}\bar{S}_{ij}}$$

The filtered strain rate tensor $\bar{S}_{ij} = (\partial_j\bar{u}_i + \partial_i\bar{u}_j)/2$ can be computed as a second moment as

$$\bar{S}_{ij} = \frac{\bar{\Sigma}_{ij}}{2\rho c_s^2 \tau_L^\star \left(1 - \frac{\omega_L \Delta t}{2}\right)} = \frac{1}{2\rho c_s^2 \tau_L^\star}\sum_\alpha e_{\alpha i} e_{\alpha j}(\bar{f}^{eq}_\alpha - \bar{f}_\alpha)$$

τ_t can be obtained as [Yu, 2004, Hou et al., 1996]

$$\tau_t = \frac{1}{2}\left(\sqrt{\tau_L^2 + 18\sqrt{2}(\rho_0 c^2)^{-1} C_{sm}^2 \Delta x |\bar{\mathbf{S}}|} - \tau_L\right)$$

Further LES models

Dynamic Smagorinsky model (DSMA)

$$C_{sm}(\mathbf{x},t)^2 = -\frac{1}{2}\frac{\langle L_{ij}M_{ij}\rangle}{\langle M_{ij}M_{ij}\rangle}$$

$$L_{ij} = T_{ij} - \widehat{\tau}_{ij} = \widehat{\overline{u}_i\overline{u}_j} - \hat{\overline{u}}_i\hat{\overline{u}}_j \qquad M_{ij} = \widehat{\Delta x}^2|\hat{\overline{\mathbf{S}}}|\hat{\overline{S}}_{ij} - \Delta x^2\widehat{|\overline{\mathbf{S}}|\overline{S}_{ij}}$$

Computations here do not use van Driest damping yet.

Further LES models

Dynamic Smagorinsky model (DSMA)

$$C_{sm}(\mathbf{x},t)^2 = -\frac{1}{2}\frac{\langle L_{ij}M_{ij}\rangle}{\langle M_{ij}M_{ij}\rangle}$$

$$L_{ij} = T_{ij} - \widehat{\tau}_{ij} = \widehat{\overline{u}_i\overline{u}_j} - \hat{\overline{u}}_i\hat{\overline{u}}_j \qquad M_{ij} = \widehat{\Delta x}^2|\hat{\overline{\mathbf{S}}}|\hat{\overline{S}}_{ij} - \Delta x^2\widehat{|\overline{\mathbf{S}}|\overline{S}_{ij}}$$

Computations here do not use van Driest damping yet.

Wall-Adapting Local Eddy-viscosity model (WALE)

$$\nu_t = (C_w\Delta x)^2 OP_{WALE}, \quad \text{where } C_w = 0.5$$

WALE turbulence time-scale

$$OP_{WALE} = \frac{(\mathcal{J}_{ij}\mathcal{J}_{ij})^{\frac{3}{2}}}{(\overline{S}_{ij}\overline{S}_{ij})^{\frac{5}{2}} + (\mathcal{J}_{ij}\mathcal{J}_{ij})^{\frac{5}{4}}}$$

$$\mathcal{J}_{ij} = \overline{S}_{ik}\overline{S}_{kj} + \overline{\Omega}_{ik}\overline{\Omega}_{kj} - \frac{1}{3}\delta_{ij}(\overline{S}_{mn}\overline{S}_{mn} - \overline{\Omega}_{mn}\overline{\Omega}_{mn})$$

Effective relaxation time (see previous slide): $\tau_L^\star = \dfrac{(\nu+\nu_t) + \Delta t c_s^2/2}{c_s^2}$

Homogeneous isotropic turbulence

- Fourier representation
- Periodic boundaries, uniform mesh
- Use of external forcing term, i.e., result independent of initial conditions

Forcing:

$$F_x = 2A\left(\frac{\kappa_y\kappa_z}{|\kappa|^2}\right)G(\kappa_x,\kappa_y,\kappa_z)$$

$$F_y = -A\left(\frac{\kappa_x\kappa_z}{|\kappa|^2}\right)G(\kappa_x,\kappa_y,\kappa_z)$$

$$F_z = -A\left(\frac{\kappa_x\kappa_y}{|\kappa|^2}\right)G(\kappa_x,\kappa_y,\kappa_z)$$

Iso-surface $||\mathbf{u}||/\langle u_{rms}\rangle = 2$

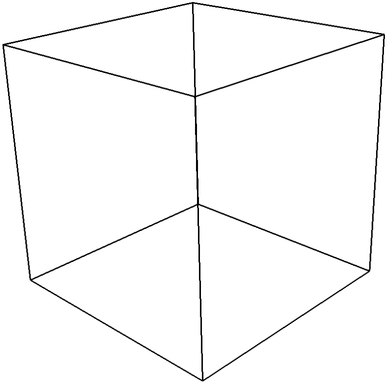

with phase

$G(\kappa_x,\kappa_y,\kappa_z) = \sin\left(\frac{2\pi x}{L}\kappa_x + \frac{2\pi y}{L}\kappa_y + \frac{2\pi z}{L}\kappa_z + \phi\right)$ for $(0 < \kappa_i \le 2)$ and ϕ being a random phase value.

Homogeneous isotropic turbulence

- Fourier representation
- Periodic boundaries, uniform mesh
- Use of external forcing term, i.e., result independent of initial conditions

Iso-surface $||\mathbf{u}||/\langle u_{rms}\rangle = 2$

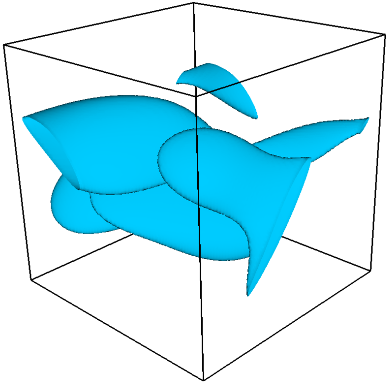

Forcing:

$$F_x = 2A\left(\frac{\kappa_y \kappa_z}{|\kappa|^2}\right) G(\kappa_x, \kappa_y, \kappa_z)$$

$$F_y = -A\left(\frac{\kappa_x \kappa_z}{|\kappa|^2}\right) G(\kappa_x, \kappa_y, \kappa_z)$$

$$F_z = -A\left(\frac{\kappa_x \kappa_y}{|\kappa|^2}\right) G(\kappa_x, \kappa_y, \kappa_z)$$

with phase

$G(\kappa_x, \kappa_y, \kappa_z) = \sin\left(\frac{2\pi x}{L}\kappa_x + \frac{2\pi y}{L}\kappa_y + \frac{2\pi z}{L}\kappa_z + \phi\right)$ for $(0 < \kappa_i \leq 2)$ and ϕ being a random phase value.

Homogeneous isotropic turbulence

- Fourier representation
- Periodic boundaries, uniform mesh
- Use of external forcing term, i.e., result independent of initial conditions

Forcing:

$$F_x = 2A\left(\frac{\kappa_y \kappa_z}{|\kappa|^2}\right) G(\kappa_x, \kappa_y, \kappa_z)$$

$$F_y = -A\left(\frac{\kappa_x \kappa_z}{|\kappa|^2}\right) G(\kappa_x, \kappa_y, \kappa_z)$$

$$F_z = -A\left(\frac{\kappa_x \kappa_y}{|\kappa|^2}\right) G(\kappa_x, \kappa_y, \kappa_z)$$

Iso-surface $||\mathbf{u}||/\langle u_{rms}\rangle = 2$

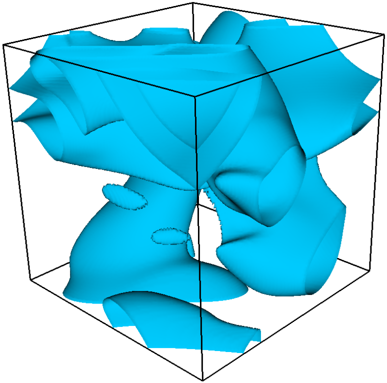

with phase

$$G(\kappa_x, \kappa_y, \kappa_z) = \sin\left(\frac{2\pi x}{L}\kappa_x + \frac{2\pi y}{L}\kappa_y + \frac{2\pi z}{L}\kappa_z + \phi\right)$$ for $(0 < \kappa_i \leq 2)$ and ϕ being a random phase value.

Homogeneous isotropic turbulence

- Fourier representation
- Periodic boundaries, uniform mesh
- Use of external forcing term, i.e., result independent of initial conditions

Iso-surface $||\mathbf{u}||/\langle u_{rms}\rangle = 2$

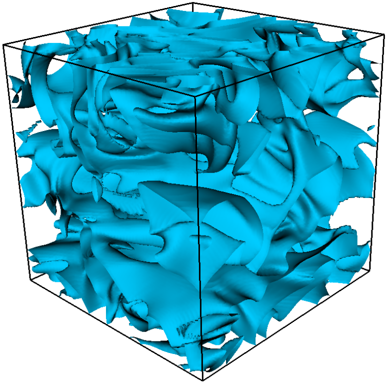

Forcing:

$$F_x = 2A\left(\frac{\kappa_y\kappa_z}{|\kappa|^2}\right)G(\kappa_x,\kappa_y,\kappa_z)$$

$$F_y = -A\left(\frac{\kappa_x\kappa_z}{|\kappa|^2}\right)G(\kappa_x,\kappa_y,\kappa_z)$$

$$F_z = -A\left(\frac{\kappa_x\kappa_y}{|\kappa|^2}\right)G(\kappa_x,\kappa_y,\kappa_z)$$

with phase

$G(\kappa_x,\kappa_y,\kappa_z) = \sin\left(\frac{2\pi x}{L}\kappa_x + \frac{2\pi y}{L}\kappa_y + \frac{2\pi z}{L}\kappa_z + \phi\right)$ for $(0 < \kappa_i \le 2)$ and ϕ being a random phase value.

Homogeneous isotropic turbulence

- Fourier representation
- Periodic boundaries, uniform mesh
- Use of external forcing term, i.e., result independent of initial conditions

Forcing:

$$F_x = 2A\left(\frac{\kappa_y \kappa_z}{|\kappa|^2}\right) G(\kappa_x, \kappa_y, \kappa_z)$$

$$F_y = -A\left(\frac{\kappa_x \kappa_z}{|\kappa|^2}\right) G(\kappa_x, \kappa_y, \kappa_z)$$

$$F_z = -A\left(\frac{\kappa_x \kappa_y}{|\kappa|^2}\right) G(\kappa_x, \kappa_y, \kappa_z)$$

Iso-surface $||\mathbf{u}||/\langle u_{rms}\rangle = 2$

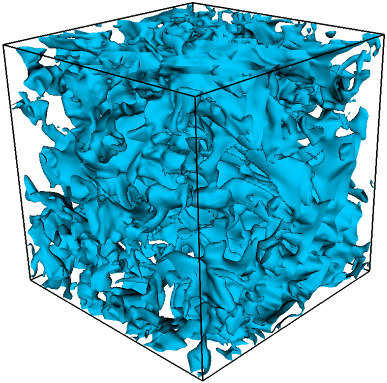

with phase

$G(\kappa_x, \kappa_y, \kappa_z) = \sin\left(\frac{2\pi x}{L}\kappa_x + \frac{2\pi y}{L}\kappa_y + \frac{2\pi z}{L}\kappa_z + \phi\right)$ for $(0 < \kappa_i \leq 2)$ and ϕ being a random phase value.

LES model verification

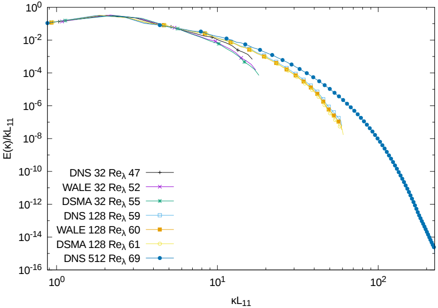

Time-averaged energy spectra normalised by the turbulent kinetic energy k and the integral length scale L_{11} of LBM DNS and LES for two resolutions and DNS of the highest resolution for the viscosity value $\nu = 5 \cdot 10^{-5}$

LES model verification

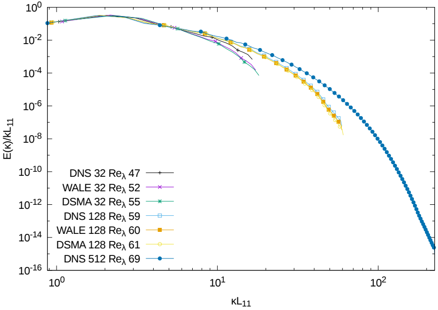

Time-averaged energy spectra normalised by the turbulent kinetic energy k and the integral length scale L_{11} of LBM DNS and LES for two resolutions and DNS of the highest resolution for the viscosity value $\nu = 5 \cdot 10^{-5}$

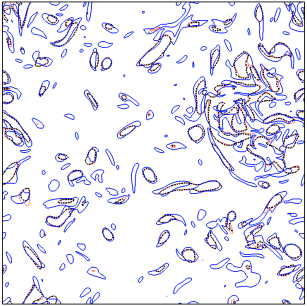

Contours of vorticity magnitude ($|\omega| = 0.18$) at $t = 68.72$ (right) for DNS (thin blue lines) of 512^3 against DSMA (dotted black lines) and WALE (thick red lines) of 128^3 cells resolution

Motion solver

Based on the Newton-Euler method solution of dynamics equation of kinetic chains [Tsai, 1999]

$$\begin{pmatrix} \mathbf{F} \\ \boldsymbol{\tau}_{\mathrm{P}} \end{pmatrix} = \begin{pmatrix} m\mathbf{1} & -m[\mathbf{c}]^{\times} \\ m[\mathbf{c}]^{\times}\mathbf{I}_{\mathrm{cm}} & -m[\mathbf{c}]^{\times}[\mathbf{c}]^{\times} \end{pmatrix} \begin{pmatrix} \mathbf{a}_{\mathrm{P}} \\ \boldsymbol{\alpha} \end{pmatrix} + \begin{pmatrix} m[\boldsymbol{\omega}]^{\times}[\boldsymbol{\omega}]^{\times}\mathbf{c} \\ [\boldsymbol{\omega}]^{\times}(\mathbf{I}_{\mathrm{cm}} - m[\mathbf{c}]^{\times}[\mathbf{c}]^{\times})\,\boldsymbol{\omega} \end{pmatrix}.$$

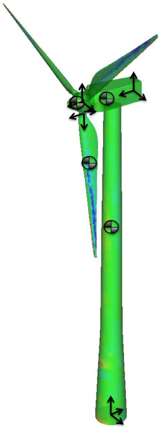

m = mass of the body, 1 = the 4×4 homogeneous identity matrix,
$\mathbf{a}_p$ = acceleration of link frame with origin at **p** in the preceding link's frame,
$\mathbf{I}_{\mathrm{cm}}$ = moment of inertia about the center of mass,
$\boldsymbol{\omega}$ = angular velocity of the body,
$\boldsymbol{\alpha}$ = angular acceleration of the body,
c is the location of the body's center of mass,
and $[\mathbf{c}]^{\times}$, $[\boldsymbol{\omega}]^{\times}$ denote skew-symmetric cross product matrices.

Motion solver

Based on the Newton-Euler method solution of dynamics equation of kinetic chains [Tsai, 1999]

$$\begin{pmatrix} \mathbf{F} \\ \boldsymbol{\tau}_\mathrm{P} \end{pmatrix} = \begin{pmatrix} m\mathbf{1} & -m[\mathbf{c}]^\times \\ m[\mathbf{c}]^\times \mathbf{I}_\mathrm{cm} & -m[\mathbf{c}]^\times[\mathbf{c}]^\times \end{pmatrix} \begin{pmatrix} \mathbf{a}_\mathrm{P} \\ \boldsymbol{\alpha} \end{pmatrix} + \begin{pmatrix} m[\boldsymbol{\omega}]^\times[\boldsymbol{\omega}]^\times \mathbf{c} \\ [\boldsymbol{\omega}]^\times(\mathbf{I}_\mathrm{cm} - m[\mathbf{c}]^\times[\mathbf{c}]^\times)\,\boldsymbol{\omega} \end{pmatrix}.$$

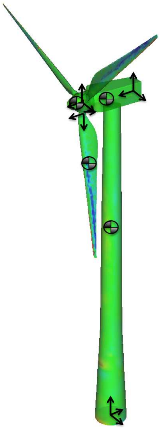

m = mass of the body, 1 = the 4×4 homogeneous identity matrix,
$\mathbf{a}_p$ = acceleration of link frame with origin at $\mathbf{p}$ in the preceding link's frame,
$\mathbf{I}_\mathrm{cm}$ = moment of inertia about the center of mass,
$\boldsymbol{\omega}$ = angular velocity of the body,
$\boldsymbol{\alpha}$ = angular acceleration of the body,
$\mathbf{c}$ is the location of the body's center of mass,
and $[\mathbf{c}]^\times$, $[\boldsymbol{\omega}]^\times$ denote skew-symmetric cross product matrices.

Here, we additionally define the total force and torque acting on a body,

$\mathbf{F} = (\mathbf{F}_{FSI} + \mathbf{F}_{prescribed}) \cdot \boldsymbol{\mathcal{C}}_{xyz}$ and

$\tau = (\tau_{FSI} + \tau_{prescribed}) \cdot \boldsymbol{\mathcal{C}}_{\alpha\beta\gamma}$ respectively.

Where $\boldsymbol{\mathcal{C}}_{xyz}$ and $\boldsymbol{\mathcal{C}}_{\alpha\beta\gamma}$ are the translational and rotational constraints, respectively.

Single Vestas V27

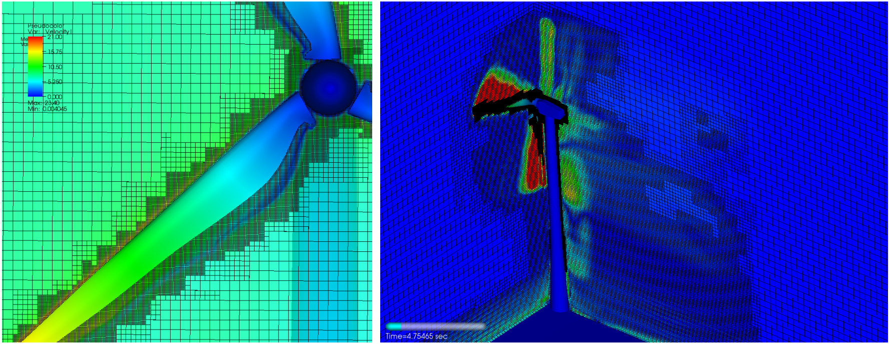

- Inflow velocity 8 $\mathrm{m/s}$. Prescribed motion of rotor with 33 rpm, $r = 14.5\,\mathrm{m}$: tip speed 46.7 $\mathrm{m/s}$, $\mathrm{Re}_r \approx 919,700$, TSR=5.84
- Simulation with three additional levels with refinement factors $2, 2, 4$
- Refinement based on vorticity and level set.
- $\sim$ 24 time steps for 1^o rotation
- Validation results: Mexico rotor [Deiterding and Wood, 2016b], [Deiterding and Wood, 2016a]

Single Vestas V27

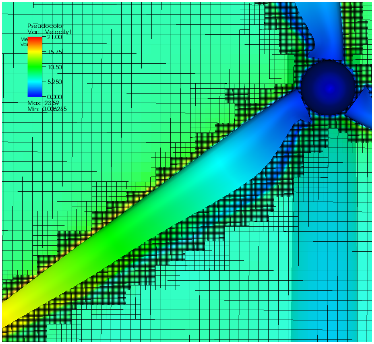

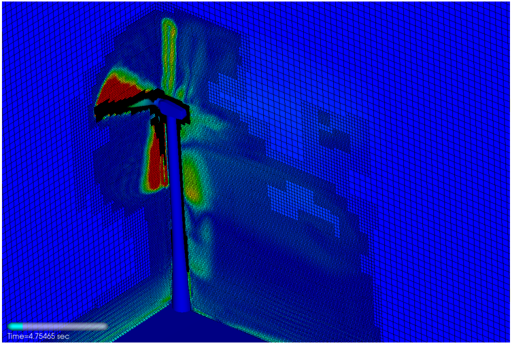

- Inflow velocity $8\,\mathrm{m/s}$. Prescribed motion of rotor with $33\,\mathrm{rpm}$, $r = 14.5\,\mathrm{m}$: tip speed $46.7\,\mathrm{m/s}$, $\mathrm{Re}_r \approx 919,700$, TSR=5.84
- Simulation with three additional levels with refinement factors $2, 2, 4$
- Refinement based on vorticity and level set.
- ~ 24 time steps for 1^o rotation
- Validation results: Mexico rotor [Deiterding and Wood, 2016b], [Deiterding and Wood, 2016a]

Single Vestas V27

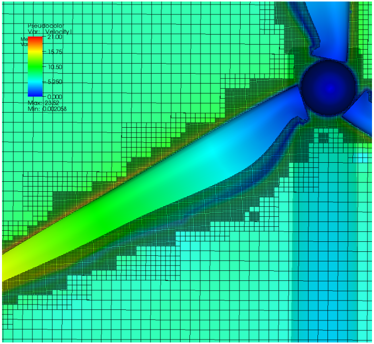

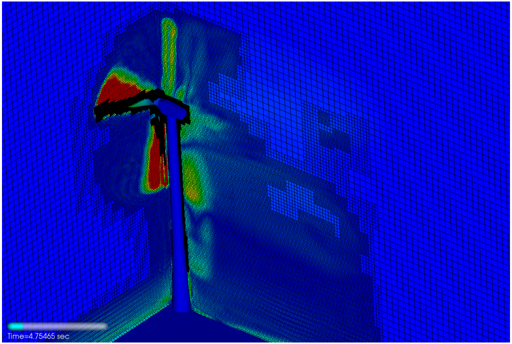

- Inflow velocity $8\,\mathrm{m/s}$. Prescribed motion of rotor with $33\,\mathrm{rpm}$, $r = 14.5\,\mathrm{m}$: tip speed $46.7\,\mathrm{m/s}$, $\mathrm{Re}_r \approx 919,700$, TSR=5.84
- Simulation with three additional levels with refinement factors $2, 2, 4$
- Refinement based on vorticity and level set.
- ~ 24 time steps for 1^o rotation
- Validation results: Mexico rotor [Deiterding and Wood, 2016b], [Deiterding and Wood, 2016a]

Single Vestas V27

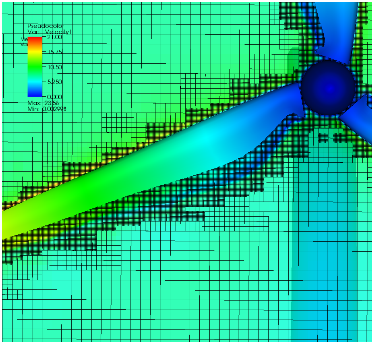

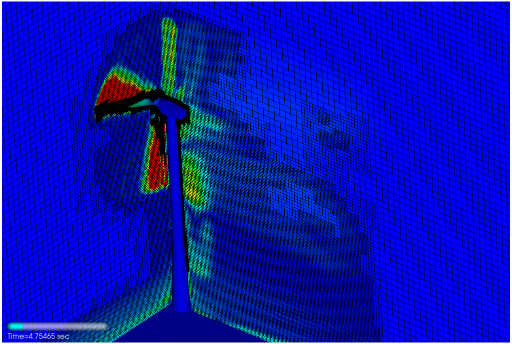

- Inflow velocity 8 $\mathrm{m/s}$. Prescribed motion of rotor with 33 rpm, $r = 14.5\,\mathrm{m}$: tip speed 46.7 $\mathrm{m/s}$, $\mathrm{Re}_r \approx 919,700$, TSR=5.84
- Simulation with three additional levels with refinement factors $2, 2, 4$
- Refinement based on vorticity and level set.
- $\sim$ 24 time steps for 1^o rotation
- Validation results: Mexico rotor [Deiterding and Wood, 2016b], [Deiterding and Wood, 2016a]

Single Vestas V27

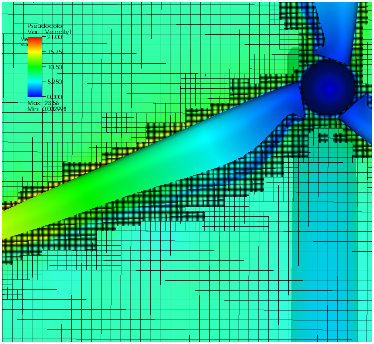

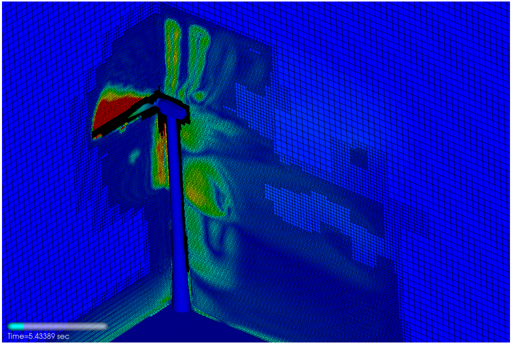

- Inflow velocity 8 $\mathrm{m/s}$. Prescribed motion of rotor with 33 rpm, $r = 14.5\,\mathrm{m}$: tip speed 46.7 $\mathrm{m/s}$, $\mathrm{Re}_r \approx 919,700$, TSR=5.84
- Simulation with three additional levels with refinement factors $2, 2, 4$
- Refinement based on vorticity and level set.
- $\sim$ 24 time steps for 1^o rotation
- Validation results: Mexico rotor [Deiterding and Wood, 2016b], [Deiterding and Wood, 2016a]

Single Vestas V27

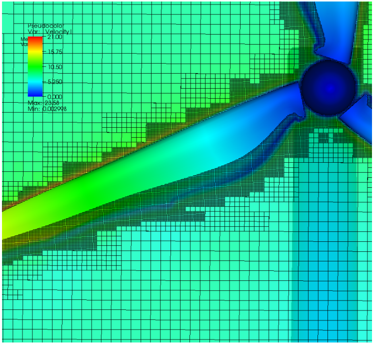

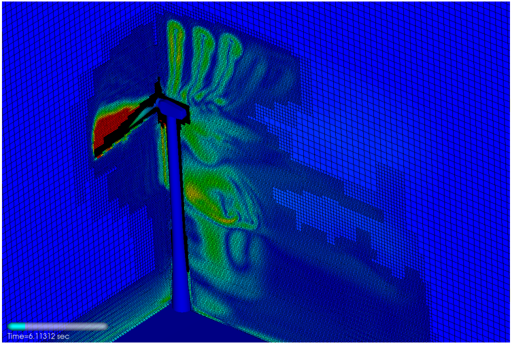

- Inflow velocity 8 $\mathrm{m/s}$. Prescribed motion of rotor with 33 rpm, $r = 14.5\,\mathrm{m}$: tip speed 46.7 $\mathrm{m/s}$, $\mathrm{Re}_r \approx 919,700$, TSR=5.84
- Simulation with three additional levels with refinement factors 2, 2, 4
- Refinement based on vorticity and level set.
- $\sim$ 24 time steps for 1^o rotation
- Validation results: Mexico rotor [Deiterding and Wood, 2016b], [Deiterding and Wood, 2016a]

Single Vestas V27

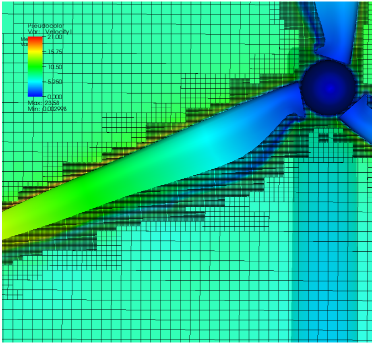

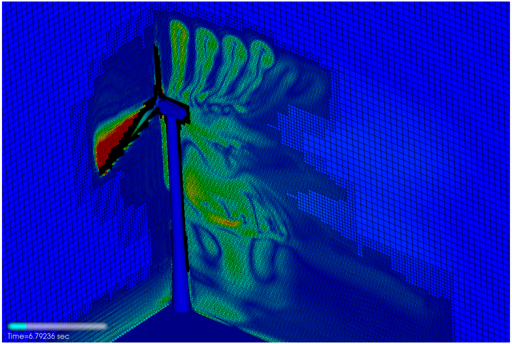

- Inflow velocity $8\,\mathrm{m/s}$. Prescribed motion of rotor with $33\,\mathrm{rpm}$, $r = 14.5\,\mathrm{m}$: tip speed $46.7\,\mathrm{m/s}$, $\mathrm{Re}_r \approx 919,700$, TSR=5.84
- Simulation with three additional levels with refinement factors $2, 2, 4$
- Refinement based on vorticity and level set.
- ~ 24 time steps for 1^o rotation
- Validation results: Mexico rotor [Deiterding and Wood, 2016b], [Deiterding and Wood, 2016a]

Single Vestas V27

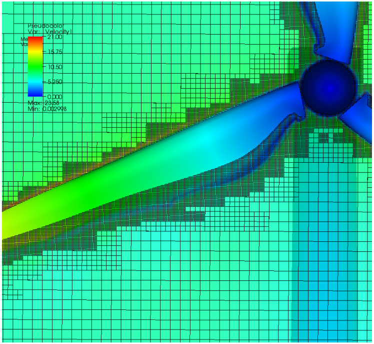

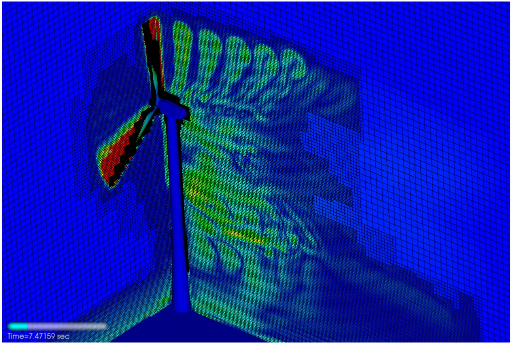

- Inflow velocity $8\,\mathrm{m/s}$. Prescribed motion of rotor with $33\,\mathrm{rpm}$, $r = 14.5\,\mathrm{m}$: tip speed $46.7\,\mathrm{m/s}$, $\mathrm{Re}_r \approx 919,700$, TSR=5.84
- Simulation with three additional levels with refinement factors $2, 2, 4$
- Refinement based on vorticity and level set.
- ~ 24 time steps for 1^o rotation
- Validation results: Mexico rotor [Deiterding and Wood, 2016b], [Deiterding and Wood, 2016a]

Single Vestas V27

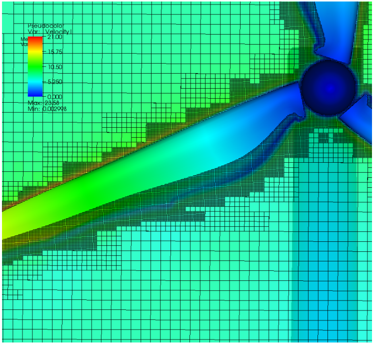

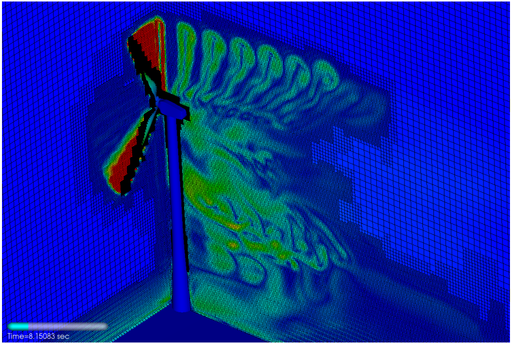

- Inflow velocity 8 $\mathrm{m/s}$. Prescribed motion of rotor with 33 rpm, $r = 14.5\,\mathrm{m}$: tip speed 46.7 $\mathrm{m/s}$, $\mathrm{Re}_r \approx 919,700$, TSR=5.84
- Simulation with three additional levels with refinement factors $2, 2, 4$
- Refinement based on vorticity and level set.
- $\sim$ 24 time steps for 1^o rotation
- Validation results: Mexico rotor [Deiterding and Wood, 2016b], [Deiterding and Wood, 2016a]

Single Vestas V27

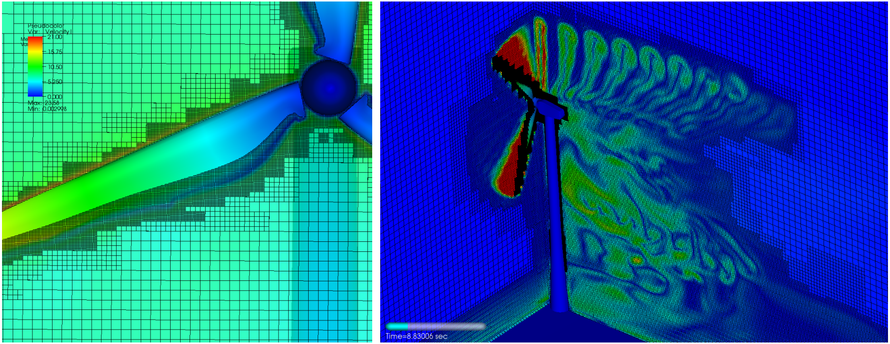

- Inflow velocity $8\,\mathrm{m/s}$. Prescribed motion of rotor with $33\,\mathrm{rpm}$, $r = 14.5\,\mathrm{m}$: tip speed $46.7\,\mathrm{m/s}$, $\mathrm{Re}_r \approx 919,700$, TSR=5.84
- Simulation with three additional levels with refinement factors $2, 2, 4$
- Refinement based on vorticity and level set.
- $\sim$ 24 time steps for 1^o rotation
- Validation results: Mexico rotor [Deiterding and Wood, 2016b], [Deiterding and Wood, 2016a]

Single Vestas V27

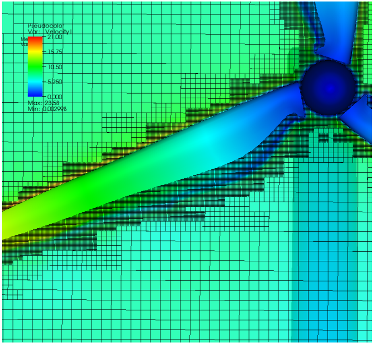

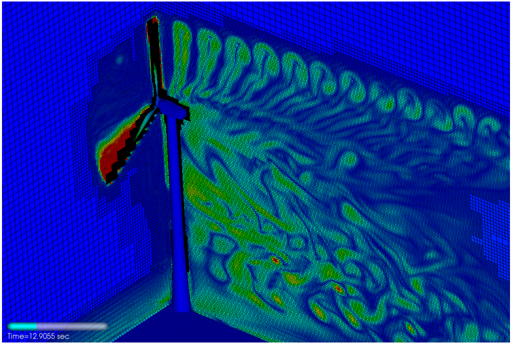

- Inflow velocity $8\,\mathrm{m/s}$. Prescribed motion of rotor with $33\,\mathrm{rpm}$, $r = 14.5\,\mathrm{m}$: tip speed $46.7\,\mathrm{m/s}$, $\mathrm{Re}_r \approx 919,700$, TSR=5.84
- Simulation with three additional levels with refinement factors $2, 2, 4$
- Refinement based on vorticity and level set.
- ~ 24 time steps for 1^o rotation
- Validation results: Mexico rotor [Deiterding and Wood, 2016b], [Deiterding and Wood, 2016a]

Single Vestas V27

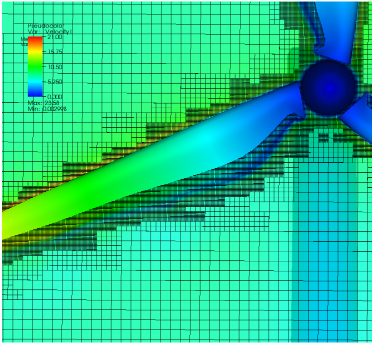

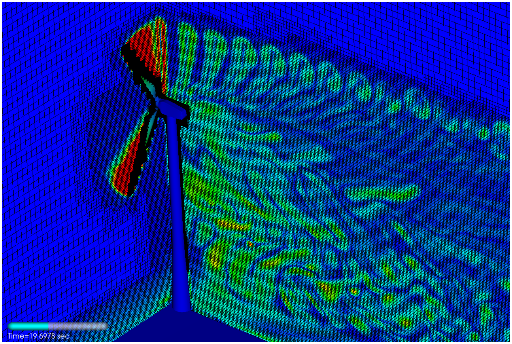

- Inflow velocity $8\,\mathrm{m/s}$. Prescribed motion of rotor with $33\,\mathrm{rpm}$, $r = 14.5\,\mathrm{m}$: tip speed $46.7\,\mathrm{m/s}$, $\mathrm{Re}_r \approx 919,700$, TSR=5.84
- Simulation with three additional levels with refinement factors $2, 2, 4$
- Refinement based on vorticity and level set.
- ~ 24 time steps for 1^o rotation
- Validation results: Mexico rotor [Deiterding and Wood, 2016b], [Deiterding and Wood, 2016a]

Rotor loads

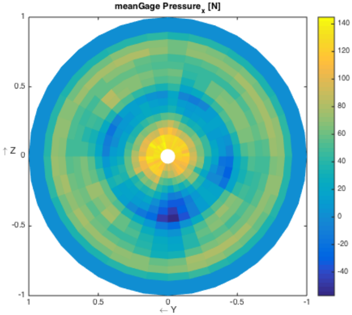

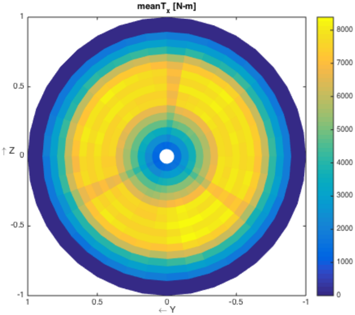

- Sampled every 0.034 s on 18 radial sections binned into 36 circumferential sectors
- Mean pressure and torque $\propto$ 81 kW production, $C_p = 0.44$, and $C_t = 0.78$
- All within 5% of the rated values [Vestas, 1994]
- A simple actuator disc model predicts 95 kW production, C_p=0.53, and C_t=0.61 for the $\bar{u}_x = 6.5\,\mathrm{m/s}$ [Schaffarczyk, 2014, Spera, 2009]

Method variation – wake vorticity field

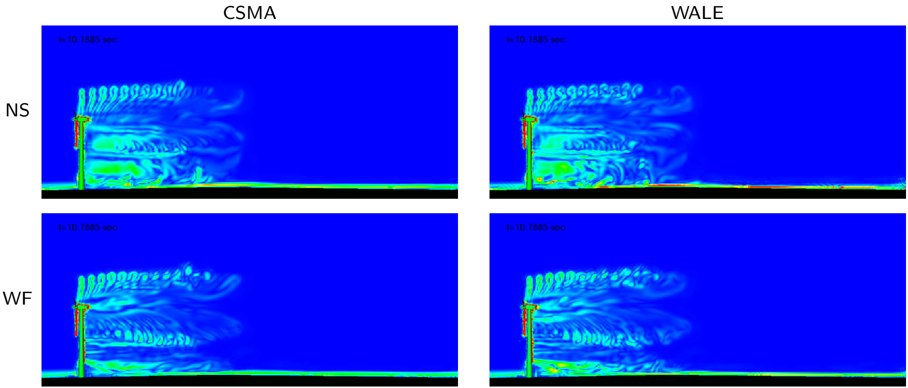

- No-slip (NS) and wall function (WF) boundary condition, const. Smagorinksy model (CSMA) with $C_{sm} = 0.14$, WALE model with $C_w = 0.5$
- D3Q27 with recursive regularized approach by [Malaspinas, 2015] up to order 6
- Simulation with three additional levels with refinement factors 2, 2, 4
- Resolution $\Delta x = 6.25\,\mathrm{cm}$ at structures, $\Delta x = 50\,\mathrm{cm}$ in wake
- $\sim 45.6\,\mathrm{s}$ in $59\,\mathrm{h}$ wall time on 80 cores Intel-Skylake 2.0 GHz ($\sim 188\,\mathrm{h}$ CPU per revolution)

Method variation – wake vorticity field

CSMA WALE

NS

WF

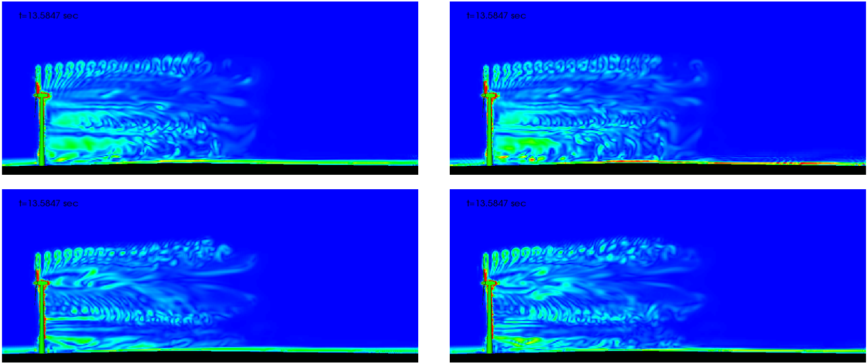

- No-slip (NS) and wall function (WF) boundary condition, const. Smagorinksy model (CSMA) with $C_{sm} = 0.14$, WALE model with $C_w = 0.5$
- D3Q27 with recursive regularized approach by [Malaspinas, 2015] up to order 6
- Simulation with three additional levels with refinement factors $2, 2, 4$
- Resolution $\Delta x = 6.25\,\mathrm{cm}$ at structures, $\Delta x = 50\,\mathrm{cm}$ in wake
- $\sim 45.6\,\mathrm{s}$ in $59\,\mathrm{h}$ wall time on 80 cores Intel-Skylake 2.0 GHz ($\sim 188\,\mathrm{h}$ CPU per revolution)

Method variation – wake vorticity field

CSMA | WALE

NS

WF

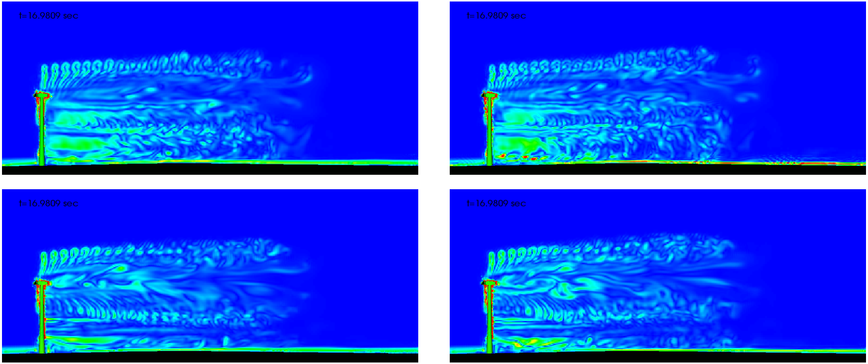

- No-slip (NS) and wall function (WF) boundary condition, const. Smagorinksy model (CSMA) with $C_{sm} = 0.14$, WALE model with $C_w = 0.5$
- D3Q27 with recursive regularized approach by [Malaspinas, 2015] up to order 6
- Simulation with three additional levels with refinement factors $2, 2, 4$
- Resolution $\Delta x = 6.25\,\mathrm{cm}$ at structures, $\Delta x = 50\,\mathrm{cm}$ in wake
- $\sim 45.6\,\mathrm{s}$ in $59\,\mathrm{h}$ wall time on 80 cores Intel-Skylake 2.0 GHz ($\sim 188\,\mathrm{h}$ CPU per revolution)

Method variation – wake vorticity field

CSMA | WALE

NS

WF

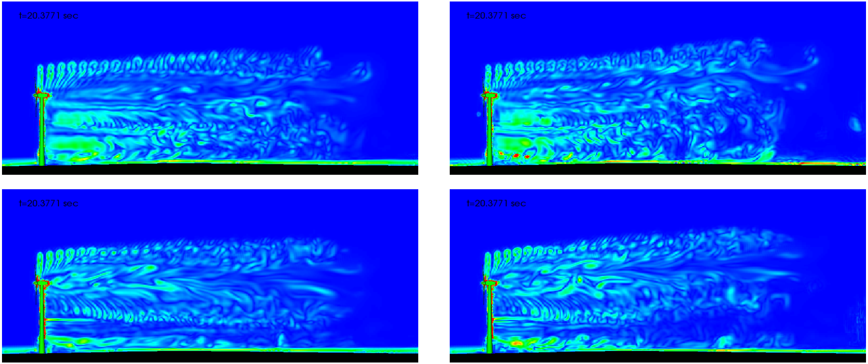

- No-slip (NS) and wall function (WF) boundary condition, const. Smagorinksy model (CSMA) with $C_{sm} = 0.14$, WALE model with $C_w = 0.5$
- D3Q27 with recursive regularized approach by [Malaspinas, 2015] up to order 6
- Simulation with three additional levels with refinement factors 2, 2, 4
- Resolution $\Delta x = 6.25\,\mathrm{cm}$ at structures, $\Delta x = 50\,\mathrm{cm}$ in wake
- $\sim 45.6\,\mathrm{s}$ in $59\,\mathrm{h}$ wall time on 80 cores Intel-Skylake 2.0 GHz ($\sim 188\,\mathrm{h}$ CPU per revolution)

Simulation of the SWIFT array

- Three prototypical Vestas V27 turbines. 225 kW power generation at wind speeds 14 to 25 $\mathrm{m/s}$ (then cut-off)
- Prescribed motion of rotor with 33 and 43 rpm. Inflow velocity 8 and 25 $\mathrm{m/s}$
- TSR: 5.84 and 2.43, $\mathrm{Re}_r \approx 919,700$ and $1,208,000$
- Simulation domain $448\,\mathrm{m} \times 240\,\mathrm{m} \times 100\,\mathrm{m}$
- Base mesh $448 \times 240 \times 100$ cells with refinement factors 2, 2, 4. Resolution of rotor and tower $\Delta x = 6.25\,\mathrm{cm}$
- 94,224 highest level iterations to 40 s computed, then statistics are gathered for 10 s [Deiterding and Wood, 2016a]

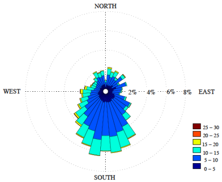

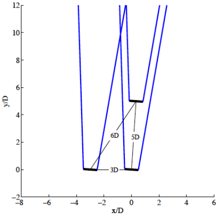

Vorticity development – inflow at 0^o, $8\,\mathrm{m/s}$, $33\,\mathrm{rpm}$

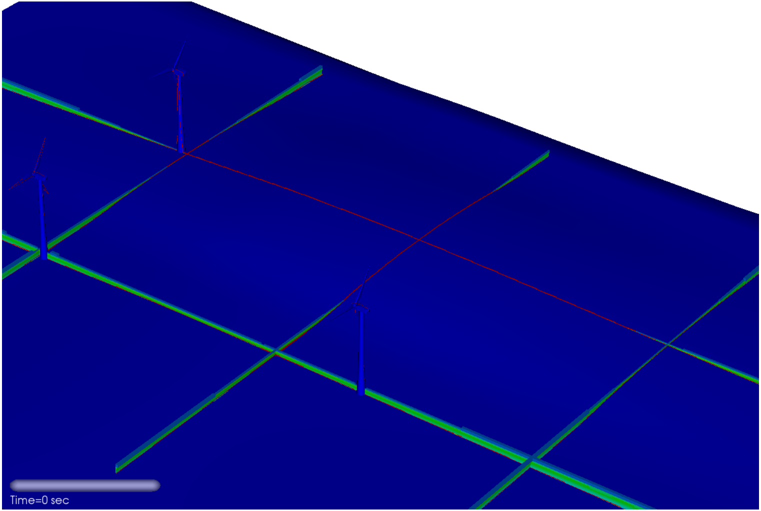

- Refinement of wake up to level 2 ($\Delta x = 25\,\mathrm{cm}$).
- Vortex break-up before 2nd turbine is reached.

Mean point values – inflow at 0^o,

- Turbines located at $(0, 0, 0)$, $(135, 0, 0)$, $(-5.65, 80.80, 0)$
- Lines of 13 sensors with $\Delta y = 5\,\mathrm{m}$, $z = 37\,\mathrm{m}$ (approx. center of rotor)
- u and p measured over $[40\,\mathrm{s}, 50\,\mathrm{s}]$ (1472 level-0 time steps) and averaged

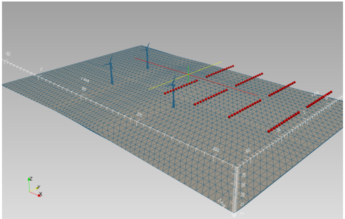

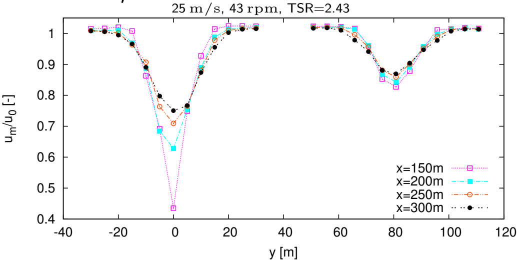

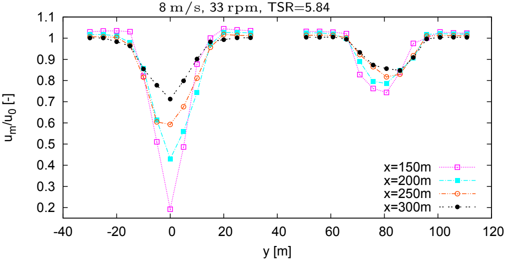

- Velocity deficits larger for higher TSR

Mean point values – inflow at 0^o,

- Turbines located at $(0, 0, 0)$, $(135, 0, 0)$, $(-5.65, 80.80, 0)$
- Lines of 13 sensors with $\Delta y = 5\,\mathrm{m}$, $z = 37\,\mathrm{m}$ (approx. center of rotor)
- u and p measured over $[40\,\mathrm{s}, 50\,\mathrm{s}]$ (1472 level-0 time steps) and averaged

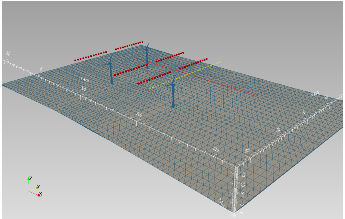

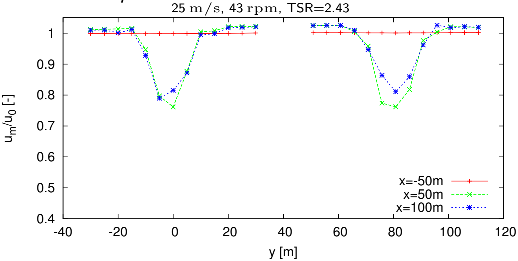

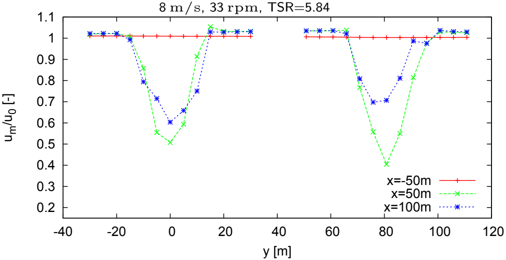

- Velocity deficits larger for higher TSR
- Velocity deficit before 2nd turbine more homogenous for small TSR

Vorticity on levels – inflow at 30^o, $8\,\mathrm{m/s}$, $33\,\mathrm{rpm}$

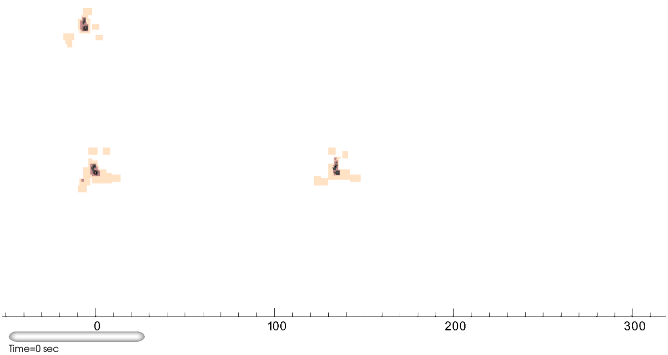

- Top view at $30\,\mathrm{m}$ (hub height). Turbine hub and inflow at 30^o yaw leads to off-axis wake impact.
- 160 cores Intel-Xeon E5 2.6 GHz, $33.03\,\mathrm{h}$ for interval $[50, 60]\,\mathrm{s}$. $\sim 320\,\mathrm{h}$ CPU per revolution and turbine
- At $63.8\,\mathrm{s}$ approximately 167M cells used vs. 44 billion (factor 264)

Level	Grids	Cells
0	2,463	10,752,000
1	6,464	20,674,760
2	39,473	131,018,832
3	827	4,909,632

Method variation – Detailed wake vorticity field

No-slip boundary condition, Constant coefficient Smagorinsky model

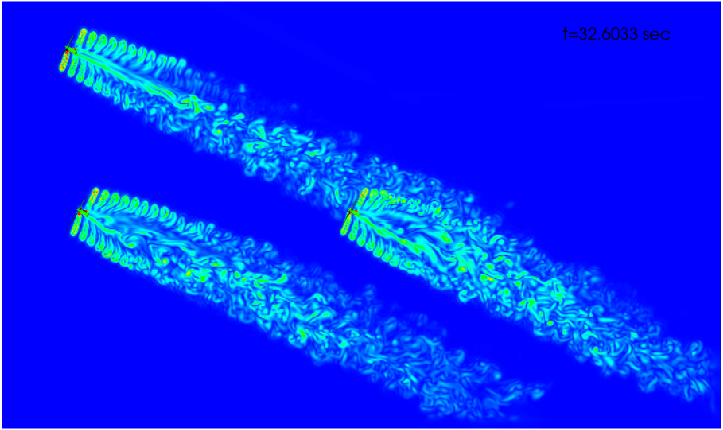

- D3Q27, CSMA with $C_{sm} = 0.14$, WALE with $C_w = 0.5$
- Lower resolution! $\Delta x = 12.5\,\mathrm{cm}$ at structures, $\Delta x = 50\,\mathrm{cm}$ in wake
- Simulation with three additional levels refined by $2, 2, 2$. Only one level for wake
- $\sim 65\,\mathrm{s}$ in $56\,\mathrm{h}$ wall time on 240 cores Intel-Skylake 2.0 GHz
- $125\,\mathrm{h}$ CPU per revolution and turbine

Method variation – Detailed wake vorticity field

Wall function boundary condition, Constant coefficient Smagorinsky model

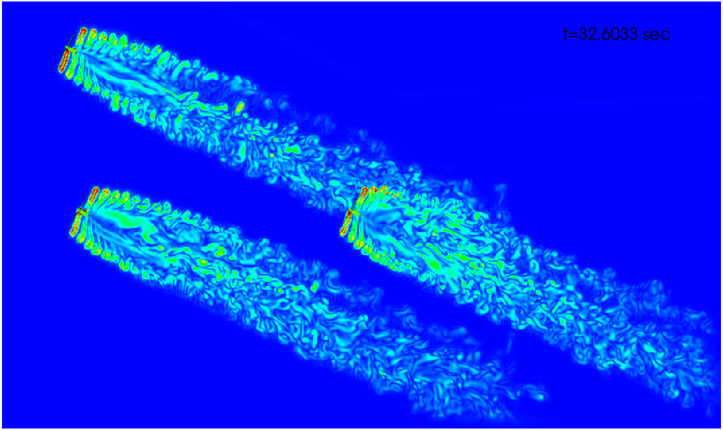

- D3Q27, CSMA with $C_{sm} = 0.14$, WALE with $C_w = 0.5$
- Lower resolution! $\Delta x = 12.5\,\mathrm{cm}$ at structures, $\Delta x = 50\,\mathrm{cm}$ in wake
- Simulation with three additional levels refined by $2, 2, 2$. Only one level for wake
- $\sim 65\,\mathrm{s}$ in $56\,\mathrm{h}$ wall time on 240 cores Intel-Skylake 2.0 GHz
- $125\,\mathrm{h}$ CPU per revolution and turbine

Method variation – Detailed wake vorticity field

Wall function boundary condition, Wall-adapting local eddy-viscosity model

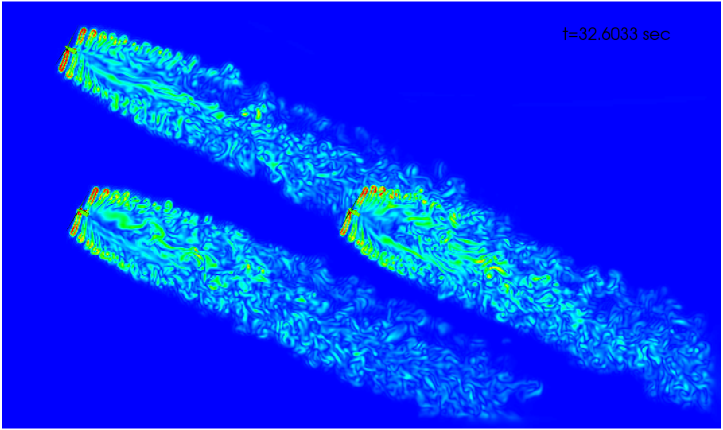

- D3Q27, CSMA with $C_{sm} = 0.14$, WALE with $C_w = 0.5$
- Lower resolution! $\Delta x = 12.5\,\mathrm{cm}$ at structures, $\Delta x = 50\,\mathrm{cm}$ in wake
- Simulation with three additional levels refined by $2, 2, 2$. Only one level for wake
- $\sim 65\,\mathrm{s}$ in $56\,\mathrm{h}$ wall time on 240 cores Intel-Skylake 2.0 GHz
- $125\,\mathrm{h}$ CPU per revolution and turbine

Method variation – Detailed wake vorticity field

No-slip boundary condition, Wall-adapting local eddy-viscosity model

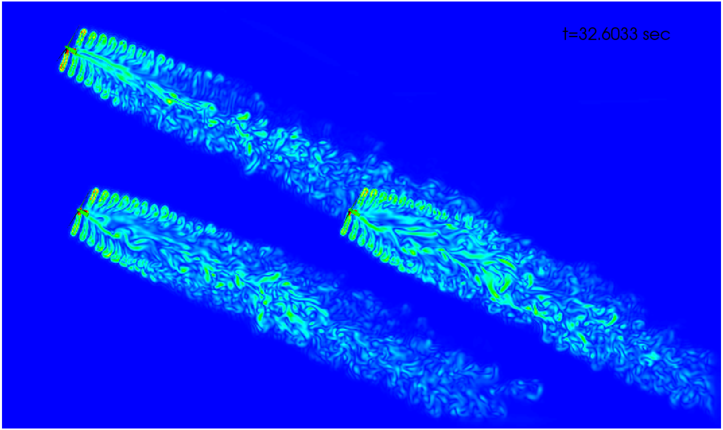

- D3Q27, CSMA with $C_{sm} = 0.14$, WALE with $C_w = 0.5$
- Lower resolution! $\Delta x = 12.5\,\mathrm{cm}$ at structures, $\Delta x = 50\,\mathrm{cm}$ in wake
- Simulation with three additional levels refined by $2, 2, 2$. Only one level for wake
- $\sim 65\,\mathrm{s}$ in $56\,\mathrm{h}$ wall time on 240 cores Intel-Skylake 2.0 GHz
- $125\,\mathrm{h}$ CPU per revolution and turbine

Method variation – 3D wake field

No-slip boundary condition, Constant coefficient Smagorinsky model

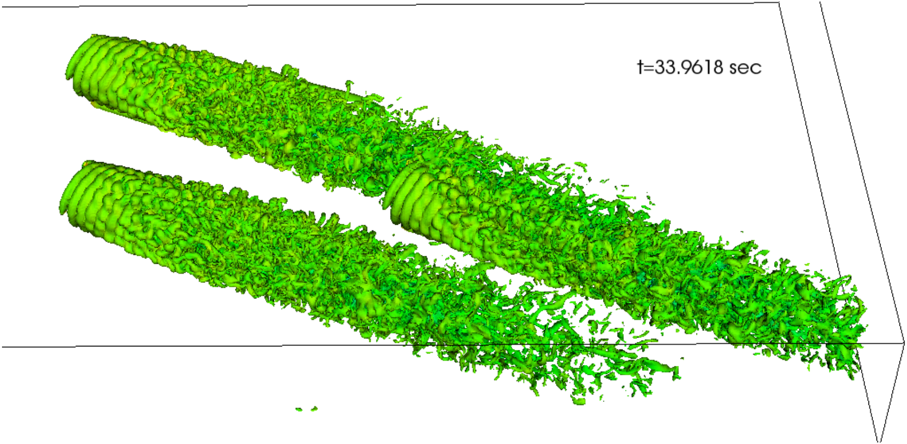

Method variation – 3D wake field

Wall function boundary condition, Constant coefficient Smagorinsky model

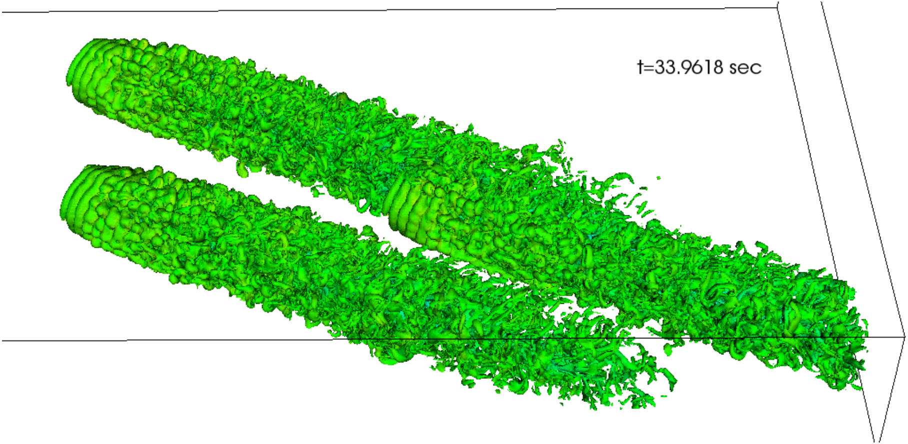

- Clearly greater extension of wake with WF boundary condition when same iso-surface value of vortcity magnitude $|\omega|$ is considered

Method variation – 3D wake field

Wall function boundary condition, Wall-adapting local eddy-viscosity model

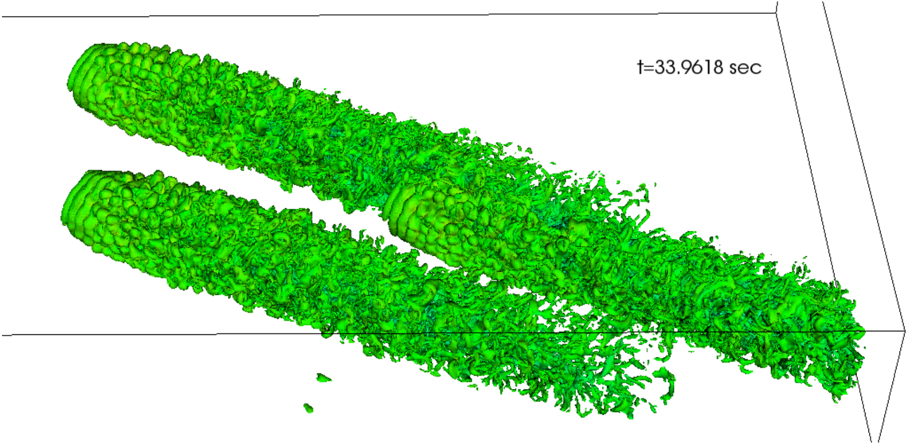

- Clearly greater extension of wake with WF boundary condition when same iso-surface value of vortcity magnitude $|\omega|$ is considered
- Slightly greater wake spread and smaller structures better preserved with WALE

Method variation – 3D wake field

No-slip boundary condition, Wall-adapting local eddy-viscosity model

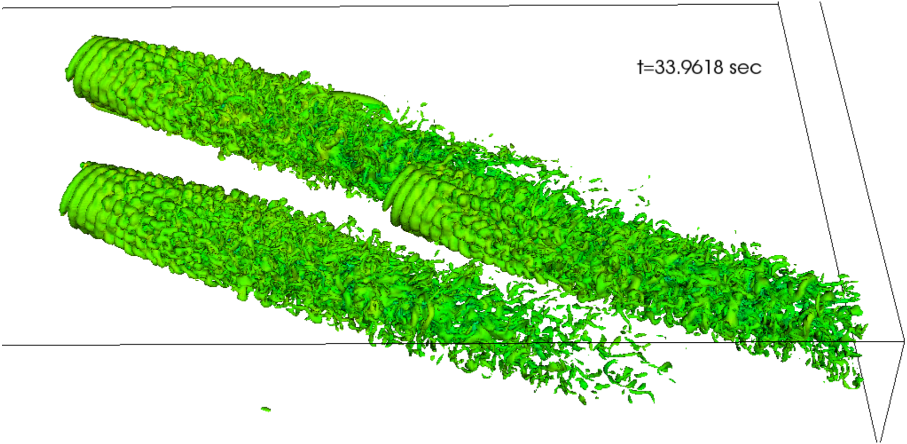

- Clearly greater extension of wake with WF boundary condition when same iso-surface value of vortcity magnitude $|\omega|$ is considered
- Slightly greater wake spread and smaller structures better preserved with WALE

Actuator line model

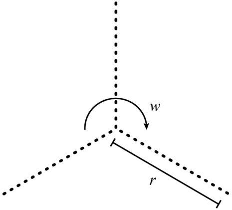

Construction of velocity U_{rel} in blade coordinate system and evaluation of local aerodynamic forces

$$L = \frac{1}{2}\rho U_{rel}^2 c C_l \partial r, \quad dD = \frac{1}{2}\rho U_{rel}^2 c C_d \partial r$$

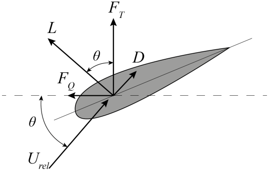

Gaussian spreading function [Sørensen et al., 1998]

$$f(d) = \frac{1}{\varepsilon^3 \pi^{\frac{3}{2}}} \; \exp\left(-\frac{d}{\varepsilon}\right)^2$$

Distance d between cell midpoint and ith actuator point

Overlapping actuator points

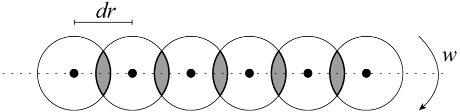

Appropriate choice of ε and dr is essential:

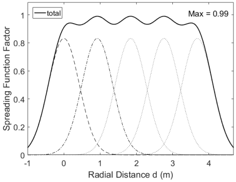

$\varepsilon = 0.6, \; dr = 0.92\,\mathrm{m}$

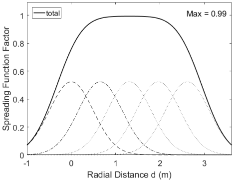

$\varepsilon = 0.7, \; dr = 0.65\,\mathrm{m}$

Simulation of single V27 rotor

- $8\,\mathrm{m/s}$, $33\,\mathrm{rpm}$, TSR: 5.84
- 3 actuator lines with 40 points. Inner radius $0.5\,\mathrm{m}$, outer radius $13.5\,\mathrm{m}$, $\varepsilon = 2\,\mathrm{m}$, $dr = 0.325\,\mathrm{m}$
- Chord length modeled roughly along actual blade
- Simulation domain $320\,\mathrm{m} \times 160\,\mathrm{m} \times 160\,\mathrm{m}$
- D3Q19 with CSMA

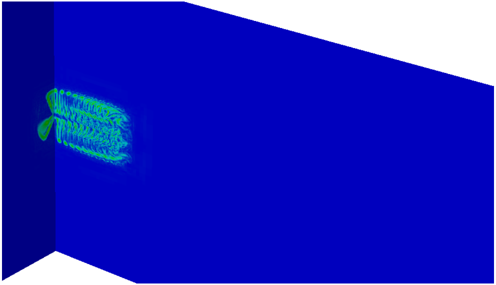

- Tip loss correction by [Shen et al., 2005] with $g = \exp[0.125(B\lambda - 21)] + 0.1$

$$F_1 = \frac{2}{\pi} \cos^{-1}\left[\exp\left(-g\,\frac{B(R-r)}{2r\sin\phi}\right)\right]$$

- Base mesh $80 \times 40 \times 40$ cells with refinement factors 2, 2, 4. Finest resolution of rotor and tower $\Delta x = 25\,\mathrm{cm}$ (same as before for wake)
- $50\,\mathrm{s}$ in $33\,\mathrm{h}$ on 12 cores Intel-Xeon-E5 2.10 GHz. $\sim 14.4\,\mathrm{h}$ CPU per revolution

Simulation of single V27 rotor

- $8\,\mathrm{m/s}$, $33\,\mathrm{rpm}$, TSR: 5.84
- 3 actuator lines with 40 points. Inner radius $0.5\,\mathrm{m}$, outer radius $13.5\,\mathrm{m}$, $\varepsilon = 2\,\mathrm{m}$, $dr = 0.325\,\mathrm{m}$
- Chord length modeled roughly along actual blade
- Simulation domain $320\,\mathrm{m} \times 160\,\mathrm{m} \times 160\,\mathrm{m}$
- D3Q19 with CSMA

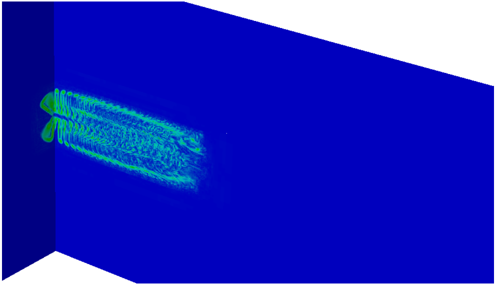

- Tip loss correction by [Shen et al., 2005] with $g = \exp[0.125(B\lambda - 21)] + 0.1$

$$F_1 = \frac{2}{\pi} \cos^{-1} \left[\exp\left(-g \frac{B(R-r)}{2r \sin\phi} \right) \right]$$

- Base mesh $80 \times 40 \times 40$ cells with refinement factors 2, 2, 4. Finest resolution of rotor and tower $\Delta x = 25\,\mathrm{cm}$ (same as before for wake)
- $50\,\mathrm{s}$ in $33\,\mathrm{h}$ on 12 cores Intel-Xeon-E5 2.10 GHz. $\sim 14.4\,\mathrm{h}$ CPU per revolution

Simulation of single V27 rotor

- $8\,\mathrm{m/s}$, $33\,\mathrm{rpm}$, TSR: 5.84
- 3 actuator lines with 40 points. Inner radius $0.5\,\mathrm{m}$, outer radius $13.5\,\mathrm{m}$, $\varepsilon = 2\,\mathrm{m}$, $dr = 0.325\,\mathrm{m}$
- Chord length modeled roughly along actual blade
- Simulation domain $320\,\mathrm{m} \times 160\,\mathrm{m} \times 160\,\mathrm{m}$
- D3Q19 with CSMA

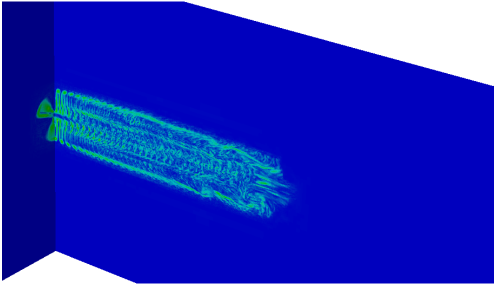

- Tip loss correction by [Shen et al., 2005] with $g = \exp[0.125(B\lambda - 21)] + 0.1$

$$F_1 = \frac{2}{\pi} \cos^{-1}\left[\exp\left(-g\,\frac{B(R-r)}{2r\sin\phi}\right)\right]$$

- Base mesh $80 \times 40 \times 40$ cells with refinement factors 2, 2, 4. Finest resolution of rotor and tower $\Delta x = 25\,\mathrm{cm}$ (same as before for wake)
- $50\,\mathrm{s}$ in $33\,\mathrm{h}$ on 12 cores Intel-Xeon-E5 2.10 GHz. $\sim 14.4\,\mathrm{h}$ CPU per revolution

Simulation of single V27 rotor

- $8\,\mathrm{m/s}$, $33\,\mathrm{rpm}$, TSR: 5.84
- 3 actuator lines with 40 points. Inner radius $0.5\,\mathrm{m}$, outer radius $13.5\,\mathrm{m}$, $\varepsilon = 2\,\mathrm{m}$, $dr = 0.325\,\mathrm{m}$
- Chord length modeled roughly along actual blade
- Simulation domain $320\,\mathrm{m} \times 160\,\mathrm{m} \times 160\,\mathrm{m}$
- D3Q19 with CSMA

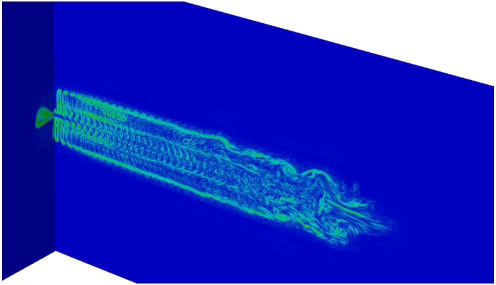

- Tip loss correction by [Shen et al., 2005] with $g = \exp[0.125(B\lambda - 21)] + 0.1$

$$F_1 = \frac{2}{\pi} \cos^{-1} \left[\exp \left(-g \frac{B(R-r)}{2r \sin \phi} \right) \right]$$

- Base mesh $80 \times 40 \times 40$ cells with refinement factors 2, 2, 4. Finest resolution of rotor and tower $\Delta x = 25\,\mathrm{cm}$ (same as before for wake)
- $50\,\mathrm{s}$ in $33\,\mathrm{h}$ on 12 cores Intel-Xeon-E5 2.10 GHz. $\sim 14.4\,\mathrm{h}$ CPU per revolution

Simulation of single V27 rotor

- $8\,\mathrm{m/s}$, $33\,\mathrm{rpm}$, TSR: 5.84
- 3 actuator lines with 40 points. Inner radius $0.5\,\mathrm{m}$, outer radius $13.5\,\mathrm{m}$, $\varepsilon = 2\,\mathrm{m}$, $dr = 0.325\,\mathrm{m}$
- Chord length modeled roughly along actual blade
- Simulation domain $320\,\mathrm{m} \times 160\,\mathrm{m} \times 160\,\mathrm{m}$
- D3Q19 with CSMA

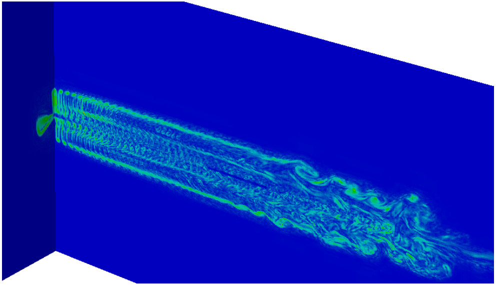

- Tip loss correction by [Shen et al., 2005] with $g = \exp[0.125(B\lambda - 21)] + 0.1$

$$F_1 = \frac{2}{\pi} \cos^{-1} \left[\exp\left(-g \frac{B(R-r)}{2r \sin\phi} \right) \right]$$

- Base mesh $80 \times 40 \times 40$ cells with refinement factors 2, 2, 4. Finest resolution of rotor and tower $\Delta x = 25\,\mathrm{cm}$ (same as before for wake)
- $50\,\mathrm{s}$ in $33\,\mathrm{h}$ on 12 cores Intel-Xeon-E5 2.10 GHz. $\sim 14.4\,\mathrm{h}$ CPU per revolution

Simulation of single V27 rotor

- $8\,\mathrm{m/s}$, $33\,\mathrm{rpm}$, TSR: 5.84
- 3 actuator lines with 40 points. Inner radius $0.5\,\mathrm{m}$, outer radius $13.5\,\mathrm{m}$, $\varepsilon = 2\,\mathrm{m}$, $dr = 0.325\,\mathrm{m}$
- Chord length modeled roughly along actual blade
- Simulation domain $320\,\mathrm{m} \times 160\,\mathrm{m} \times 160\,\mathrm{m}$
- D3Q19 with CSMA

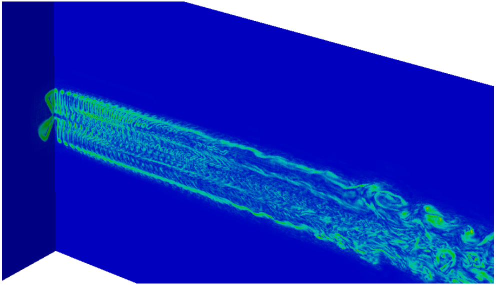

- Tip loss correction by [Shen et al., 2005] with $g = \exp[0.125(B\lambda - 21)] + 0.1$

$$F_1 = \frac{2}{\pi} \cos^{-1}\left[\exp\left(-g\frac{B(R-r)}{2r\sin\phi}\right)\right]$$

- Base mesh $80 \times 40 \times 40$ cells with refinement factors 2, 2, 4. Finest resolution of rotor and tower $\Delta x = 25\,\mathrm{cm}$ (same as before for wake)
- $50\,\mathrm{s}$ in $33\,\mathrm{h}$ on 12 cores Intel-Xeon-E5 2.10 GHz. $\sim 14.4\,\mathrm{h}$ CPU per revolution

Simulation of single V27 rotor

- 8 $\mathrm{m/s}$, 33 rpm, TSR: 5.84
- 3 actuator lines with 40 points. Inner radius 0.5 m, outer radius 13.5 m, $\varepsilon = 2\,\mathrm{m}$, $dr = 0.325\,\mathrm{m}$
- Chord length modeled roughly along actual blade
- Simulation domain 320 $\mathrm{m} \times 160\,\mathrm{m} \times 160\,\mathrm{m}$
- D3Q19 with CSMA

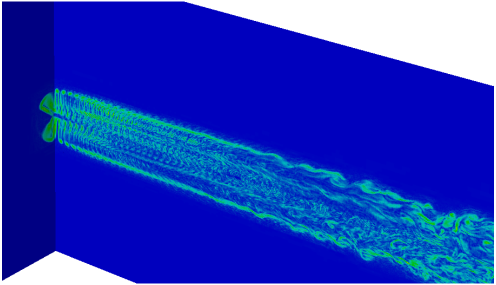

- Tip loss correction by [Shen et al., 2005] with $g = \exp[0.125(B\lambda - 21)] + 0.1$

$$F_1 = \frac{2}{\pi} \cos^{-1} \left[\exp \left(-g \frac{B(R-r)}{2r \sin \phi} \right) \right]$$

- Base mesh $80 \times 40 \times 40$ cells with refinement factors 2, 2, 4. Finest resolution of rotor and tower $\Delta x = 25\,\mathrm{cm}$ (same as before for wake)
- 50 s in 33 h on 12 cores Intel-Xeon-E5 2.10 GHz. $\sim$ 14.4 h CPU per revolution

Axial velocity profiles at $t = 43\,\mathrm{s}$

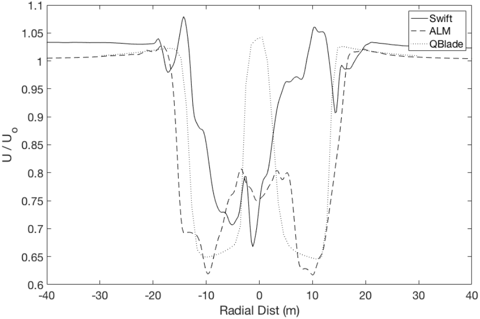

At hub height 100m downstream

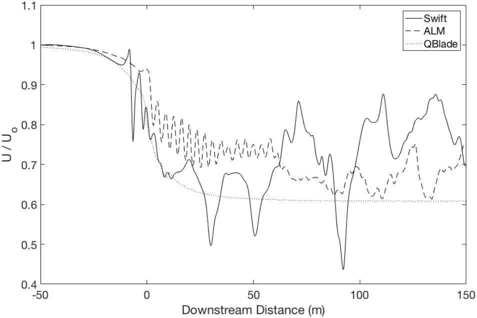

Downstream at rotor center

- Reasonable quantitative agreement in averaged axial velocity
- Smaller scale wake structures imminently different than with resolved geometry approach

Conclusions

- Thanks to the low dissipation property of the LBM wake convection behavior is excellent. Hierachical meshes are crucial for efficiency.

Conclusions

- Thanks to the low dissipation property of the LBM wake convection behavior is excellent. Hierachical meshes are crucial for efficiency.
- Conventional standard D3Q19 performs very similar to recursive regularized D3Q27 when run under stable conditions.

Conclusions

- Thanks to the low dissipation property of the LBM wake convection behavior is excellent. Hierachical meshes are crucial for efficiency.
- Conventional standard D3Q19 performs very similar to recursive regularized D3Q27 when run under stable conditions.
- Influence of LES turbulence models when starting from laminar inflow is small for our test configuration.

Conclusions

- Thanks to the low dissipation property of the LBM wake convection behavior is excellent. Hierachical meshes are crucial for efficiency.
- Conventional standard D3Q19 performs very similar to recursive regularized D3Q27 when run under stable conditions.
- Influence of LES turbulence models when starting from laminar inflow is small for our test configuration.
- Simple embedded no-slip and wall function boundary conditions give quite similar results on the hiearchical Cartesian mesh.
    - Error in geometry representation on Cartesian mesh dominant. Finite volume LBM can eliminate this problem.

Conclusions

- Thanks to the low dissipation property of the LBM wake convection behavior is excellent. Hierachical meshes are crucial for efficiency.
- Conventional standard D3Q19 performs very similar to recursive regularized D3Q27 when run under stable conditions.
- Influence of LES turbulence models when starting from laminar inflow is small for our test configuration.
- Simple embedded no-slip and wall function boundary conditions give quite similar results on the hiearchical Cartesian mesh.
    - Error in geometry representation on Cartesian mesh dominant. Finite volume LBM can eliminate this problem.
- Actuator line approach is at least O(10) faster than resolving geometry.
    - Modelling challenges for medium and small-scale turbulent wake structures are imminent.
    - Consideration of tower and ground topology can pose stability challenges.

Conclusions

- Thanks to the low dissipation property of the LBM wake convection behavior is excellent. Hierachical meshes are crucial for efficiency.
- Conventional standard D3Q19 performs very similar to recursive regularized D3Q27 when run under stable conditions.
- Influence of LES turbulence models when starting from laminar inflow is small for our test configuration.
- Simple embedded no-slip and wall function boundary conditions give quite similar results on the hiearchical Cartesian mesh.
  - Error in geometry representation on Cartesian mesh dominant. Finite volume LBM can eliminate this problem.
- Actuator line approach is at least O(10) faster than resolving geometry.
  - Modelling challenges for medium and small-scale turbulent wake structures are imminent.
  - Consideration of tower and ground topology can pose stability challenges.
- Immediate next steps: Test synthetic eddy inflow conditions and dynamic Smagorinsky LES model with van Driest damping.

References I

[Chiu et al., 2010] Chiu, P. H., Lin, R. K., and Sheu, T. W. (2010). A differentially interpolated direct forcing immersed boundary method for predicting incompressible Navier-Stokes equations in time-varying complex geometries. *Journal of Computational Physics*, 229:4476–4500.

[Deiterding, 2011] Deiterding, R. (2011). Block-structured adaptive mesh refinement - theory, implementation and application. *European Series in Applied and Industrial Mathematics: Proceedings*, 34:97–150.

[Deiterding et al., 2007] Deiterding, R., Cirak, F., Mauch, S. P., and Meiron, D. I. (2007). A virtual test facility for simulating detonation- and shock-induced deformation and fracture of thin flexible shells. *Int. J. Multiscale Computational Engineering*, 5(1):47–63.

[Deiterding et al., 2006] Deiterding, R., Radovitzky, R., Mauch, S. P., Noels, L., Cummings, J. C., and Meiron, D. I. (2006). A virtual test facility for the efficient simulation of solid materials under high energy shock-wave loading. *Engineering with Computers*, 22(3-4):325–347.

[Deiterding and Wood, 2015] Deiterding, R. and Wood, S. L. (2015). A dynamically adaptive lattice Boltzmann method for predicting wake phenomena in fully coupled wind engineering problems. In Schrefler, B., Onate, E., and Papadrakakis, M., editors, *IV Int. Conf. on Coupled Problems in Science and Engineering*, pages 489–500.

[Deiterding and Wood, 2016a] Deiterding, R. and Wood, S. L. (2016a). An adaptive lattice Boltzmann method for predicting wake fields behind wind turbines. In Dillmann, A., Heller, G., Krämer, E., Wagner, C., and Breitsamter, C., editors, *New Results in Numerical and Experimental Fluid Mechanics X*, volume 132 of *Notes on Numerical Fluid Mechanics and Multidisciplinary Design*, pages 845–857. Springer.

[Deiterding and Wood, 2016b] Deiterding, R. and Wood, S. L. (2016b). Predictive wind turbine simulation with an adaptive lattice Boltzmann method for moving boundaries. *J. Phys. Conf. Series*, 753:082005.

[Hou et al., 1996] Hou, S., Sterling, J., Chen, S., and Doolen, G. D. (1996). A lattice Boltzmann subgrid model for high Reynolds number flows. In Lawniczak, A. T. and Kapral, R., editors, *Pattern formation and lattice gas automata*, volume 6, pages 151–166. Fields Inst Comm.

[Malaspinas, 2015] Malaspinas, O. (2015). Increasing stability and accuracy of the lattice boltzmann scheme: recursivity and regularization.

[Mauch, 2000] Mauch, S. (2000). A fast algorithm for computing the closest point and distance transform. *SIAM J. Scientific Comput.*

[Reyes Barraza and Deiterding, 2020] Reyes Barraza, J. A. and Deiterding, R. (2020). Towards a generalised lattice boltzmann method for aerodynamic simulations. *J. Computational Science*, 45:101182.

References II

[Schaffarczyk, 2014] Schaffarczyk, A. P. (2014). *Introduction to Wind Turbine Aerodynamics*. Springer-Verlag, Berlin Heidelberg, Germany.

[Shen et al., 2005] Shen, W. Z., Mikkelsen, R., Sørensen, J. N., and Bak, C. (2005). Tip loss corrections for wind turbine computations. *Wind Energy*, 8(4):457–475.

[Sørensen et al., 1998] Sørensen, J. N., Shen, W. Z., and Munduate, X. (1998). Analysis of wake states by a full-field actuator disc model. *Wind Energy*, 1(2):73–88.

[Spera, 2009] Spera, D. A., editor (2009). *Wind Turbine Technology*. ASME, New York.

[Tsai, 1999] Tsai, L. (1999). *Robot Analysis: The Mechanics of Serial and Parallel Manipulators*. Wiley.

[Vestas, 1994] Vestas (1994). V27-225 kw, 50 hz wind turbine with tubular/lattice tower. Research Report 941129 1.2.0.24, Vestas.

[Yu, 2004] Yu, H. (2004). *Lattice Boltzmann equation simulations of turbulence, mixing, and combustion*. PhD thesis, Texas A&M University.

Lattice Boltzmann equation in mapped coordinates

Solves lattice Boltzmann equation in mapped coordinates

$$\frac{\partial f}{\partial t} + \tilde{e}_{\alpha\xi}\frac{\partial f_\alpha}{\partial \xi} + \tilde{e}_{\alpha\eta}\frac{\partial f_\alpha}{\partial \eta} = -\frac{1}{\tau}\left(f_\alpha - f_\alpha^{eq}\right).$$

by applying finite volume scheme (2nd-order central differences with 4th-order dissipation stabilization) to transport step. Collision step unchanged [Reyes Barraza and Deiterding, 2020].

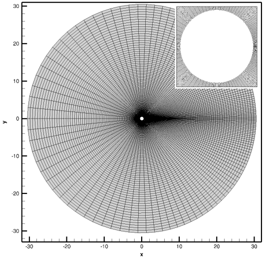

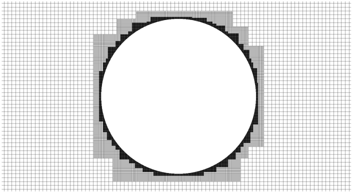

Re	Author(s)	St	$\overline{C_d}$	C_l'
100	[Chiu et al., 2010]	0.167	1.35	0.30
	AMROC-LBM	0.166	1.28	0.32
	FV-LBM	0.165	1.36	0.35
200	[Chiu et al., 2010]	0.198	1.37	0.71
	AMROC-LBM	0.196	1.26	0.70
	FV-LBM	0.196	1.37	0.73

Re		CPU-time	Mesh
20	AMROC-LBM	24:55:21	297796
	FV-LBM	06:08:41	65536
40	AMROC-LBM	27:10:08	317732
	FV-LBM	05:57:17	65536
100	AMROC-LBM	113:15:37	1026116
	FV-LBM	05:58:49	65536
200	AMROC-LBM	130:37:18	1130212
	FV-LBM	06:03:42	65536

Results

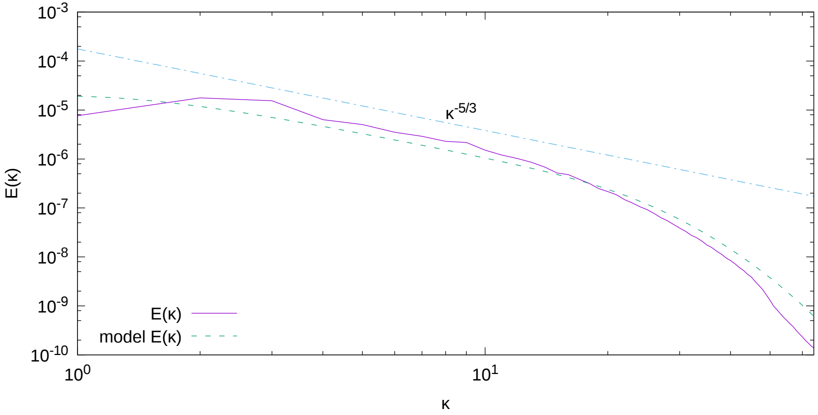

Time-averaged energy spectrum (solid line) [$N = 128^3$ cells, $\nu = 3e^{-5}\ \mathrm{m}^2/\mathrm{s}$] against a modelled one (dashed line and the -5/3 power law (dot-dashed line).

Near wake pressures

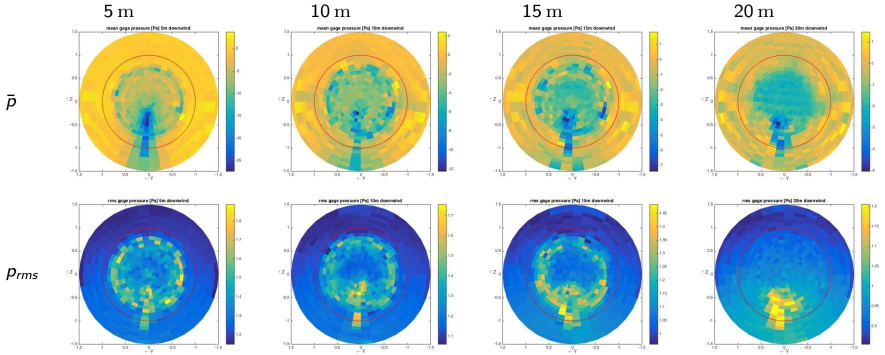

- Sampled every 0.034 s on 6 circular regions centered at hub height ($r_c = 1.5R$)
- 20 radial positions on 36 circumferential sectors
- Tower shadow prominent
- $\bar{p}$ deficit recovers 60% by 20 m

Near wake pressures

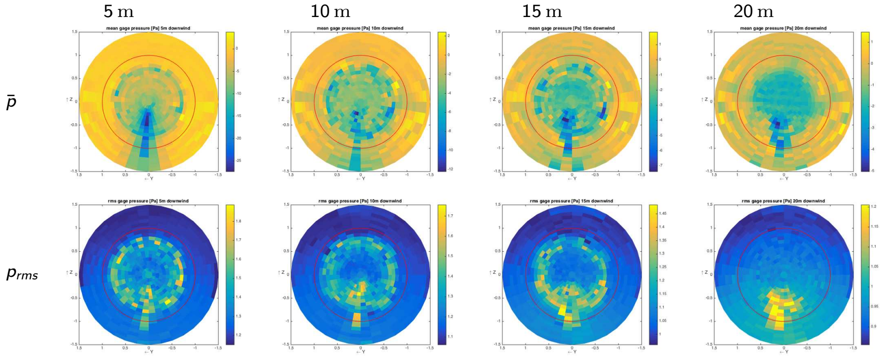

- Sampled every $0.034\,\mathrm{s}$ on 6 circular regions centered at hub height ($r_c = 1.5R$)
- 20 radial positions on 36 circumferential sectors
- Tower shadow prominent
- $\bar{p}$ deficit recovers 60% by $20\,\mathrm{m}$
- p_{rms} deficit recovers 22% by $20\,\mathrm{m}$
- p_{rms} most intense in tower shadow

Detailed wake vorticity field

No-slip boundary condition, Constant coefficient Smagorinsky model

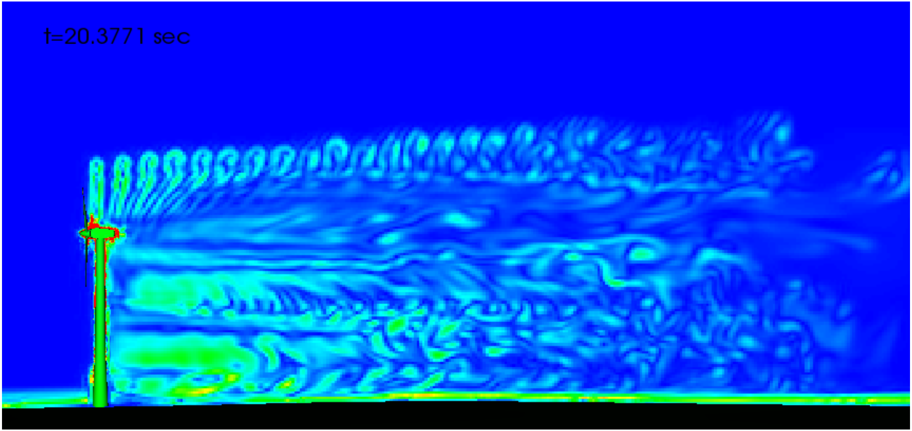

Detailed wake vorticity field

Wall function boundary condition, Constant coefficient Smagorinsky model

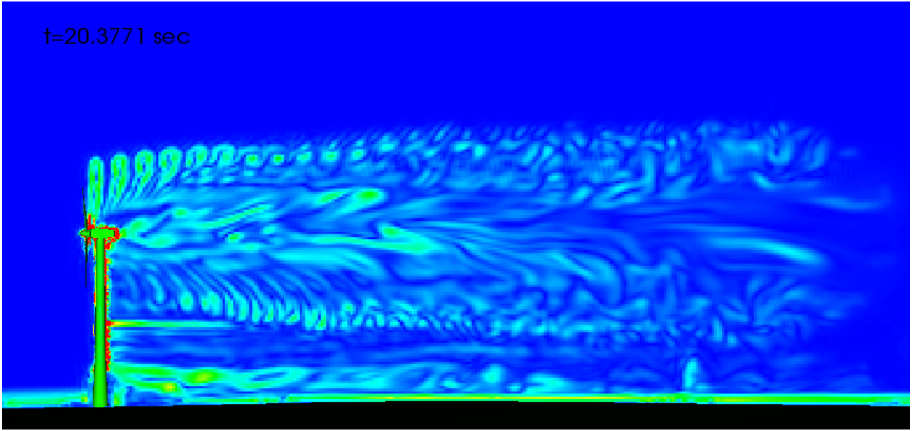

- Stronger, more stable vortices with no-slip boundary condition from blade rotation and behind tower

Detailed wake vorticity field

Wall function boundary condition, Wall-adapting local eddy-viscosity model

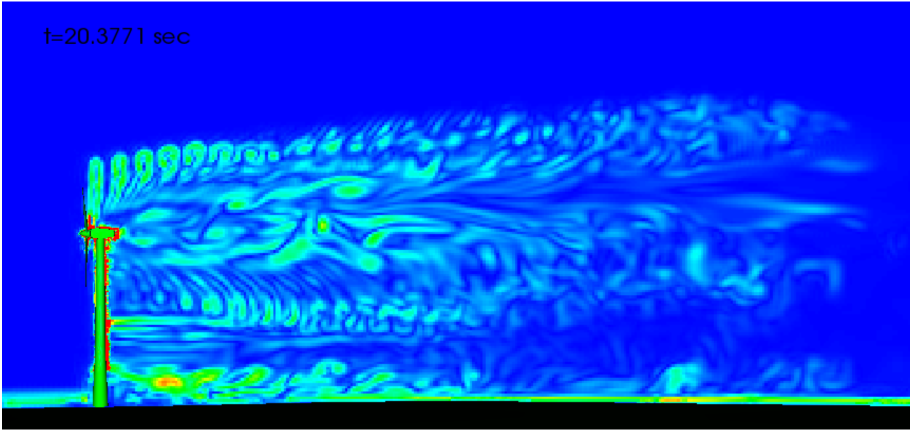

- Stronger, more stable vortices with no-slip boundary condition from blade rotation and behind tower
- Slightly larger expansion of downstream wake with WALE model than with CSMA

Detailed wake vorticity field

No-slip boundary condition, Wall-adapting local eddy-viscosity model

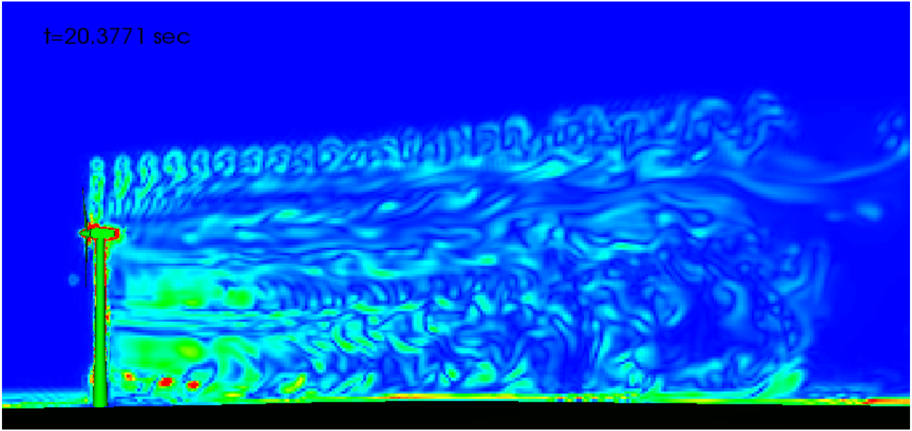

- Stronger, more stable vortices with no-slip boundary condition from blade rotation and behind tower
- Slightly larger expansion of downstream wake with WALE model than with CSMA

Refinement – inflow at 0^o, $8\,\mathrm{m/s}$, $33\,\mathrm{rpm}$

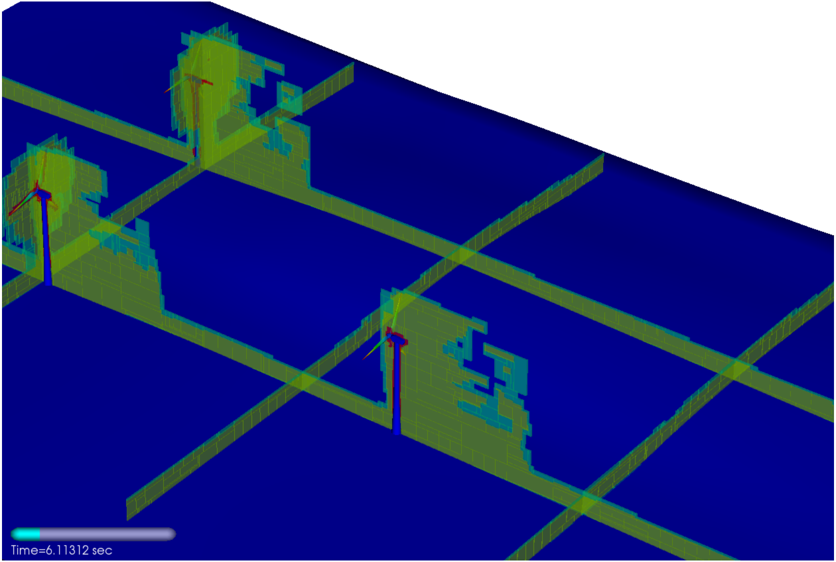

Refinement – inflow at 0^o, $8\,\mathrm{m/s}$, $33\,\mathrm{rpm}$

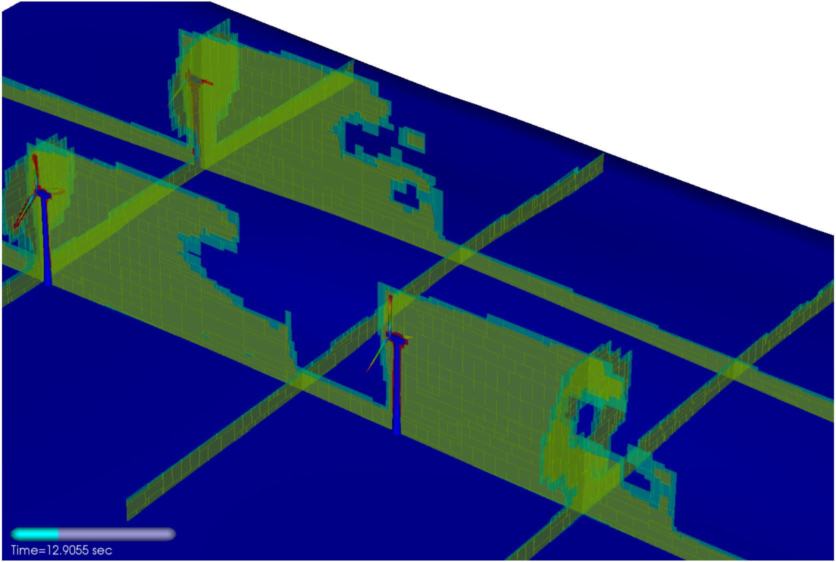

Refinement – inflow at 0^o, $8\,\mathrm{m/s}$, $33\,\mathrm{rpm}$

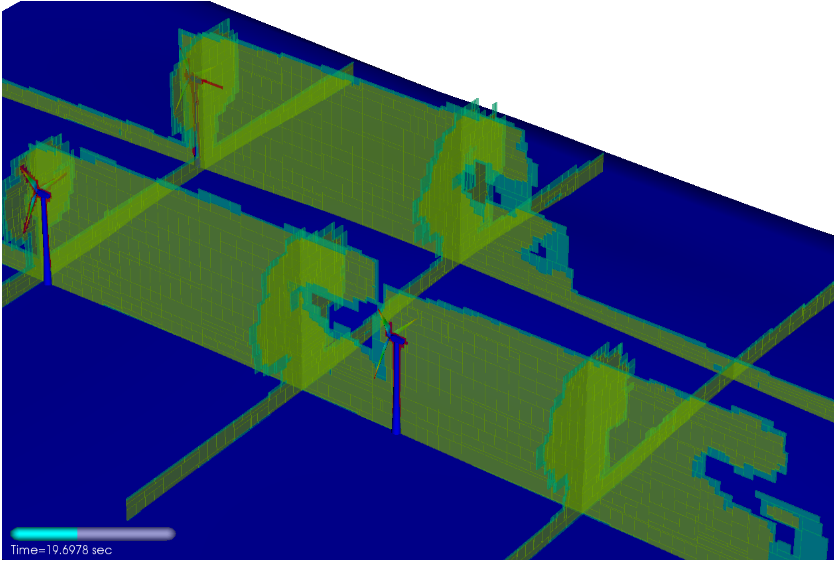

Refinement – inflow at 0^o, $8\,\mathrm{m/s}$, $33\,\mathrm{rpm}$

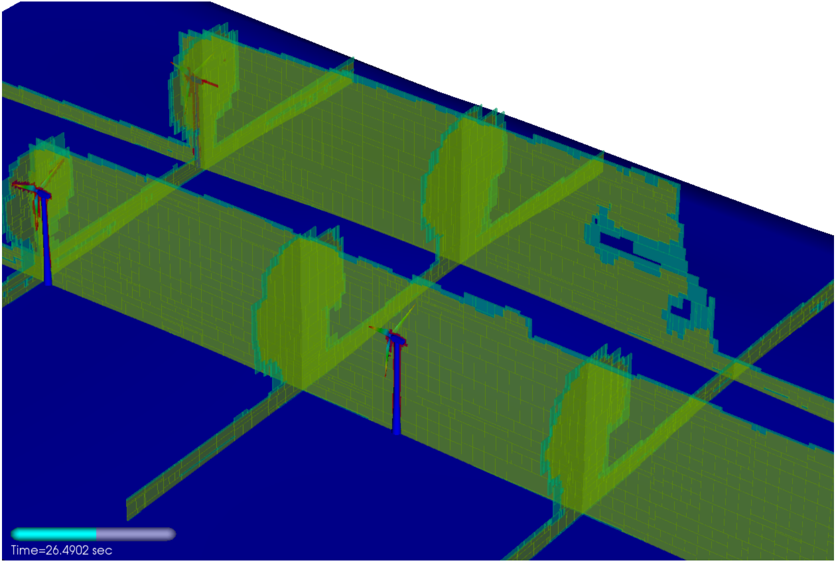

Refinement – inflow at 0°, $8\,\mathrm{m/s}$, $33\,\mathrm{rpm}$

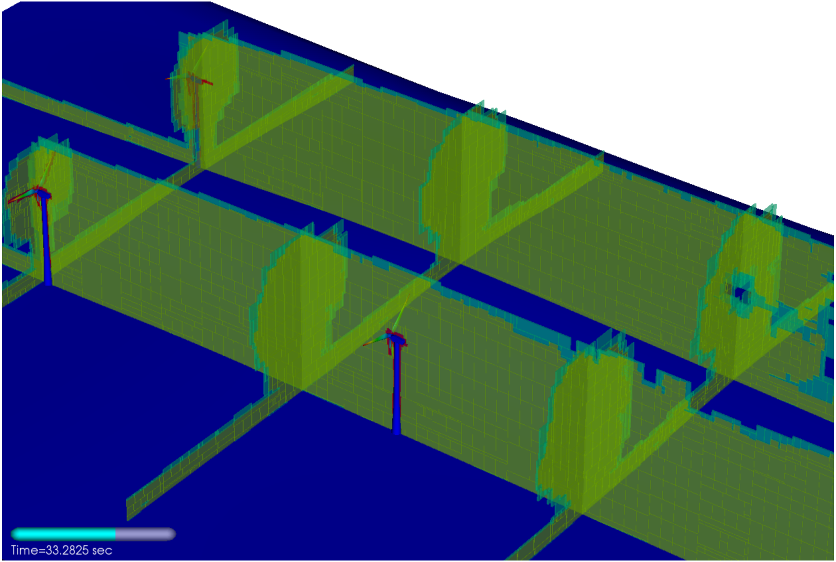

Refinement – inflow at 0^o, $8\,\mathrm{m/s}$, $33\,\mathrm{rpm}$

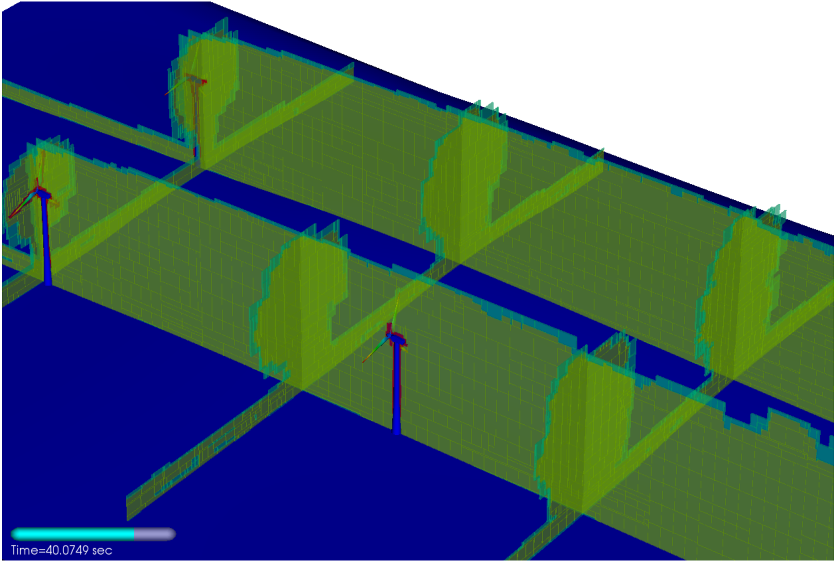

Vorticity – inflow at 30^o, $8\,\mathrm{m/s}$, $33\,\mathrm{rpm}$

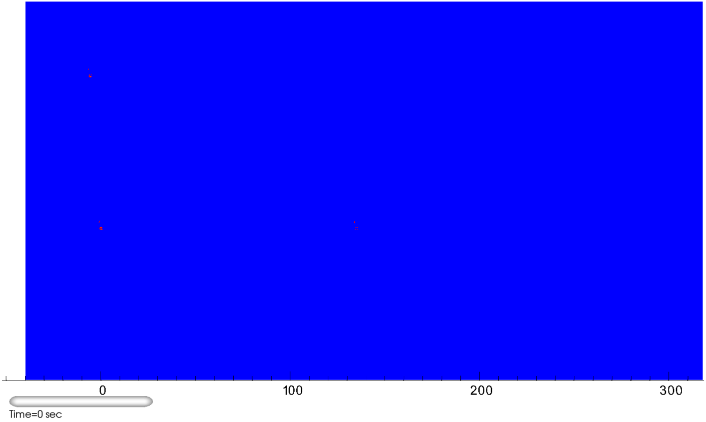

- Top view in plane in z-direction at $30\,\mathrm{m}$ (hub height)
- Turbine hub and inflow at 30^o yaw leads to off-axis wake impact.
- 160 cores Intel-Xeon E5 2.6 GHz, $33.03\,\mathrm{h}$ wall time for interval $[50, 60]\,\mathrm{s}$ (including gathering of statistical data)

Method variation – Wake vorticity field

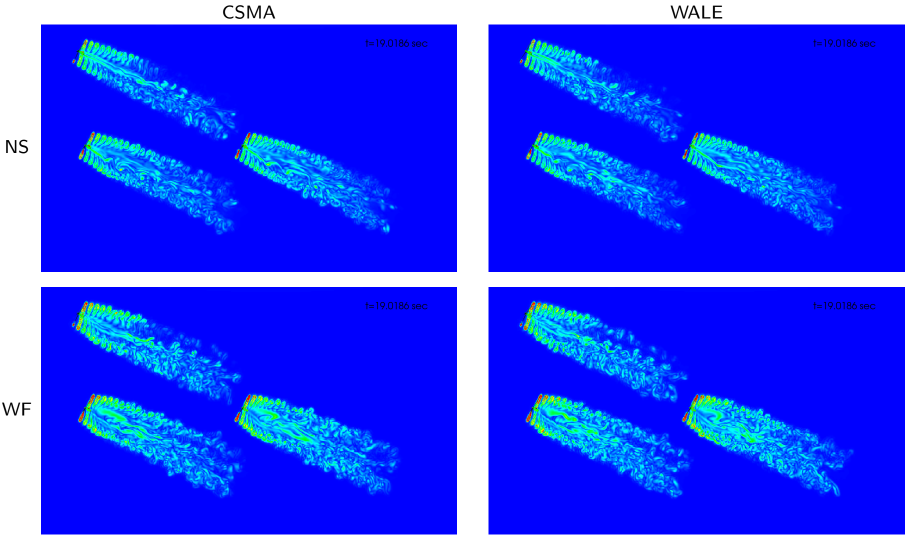

- D3Q27, CSMA with $C_{sm} = 0.14$, WALE with $C_W = 0.5$

Method variation – Wake vorticity field

CSMA WALE

NS

WF

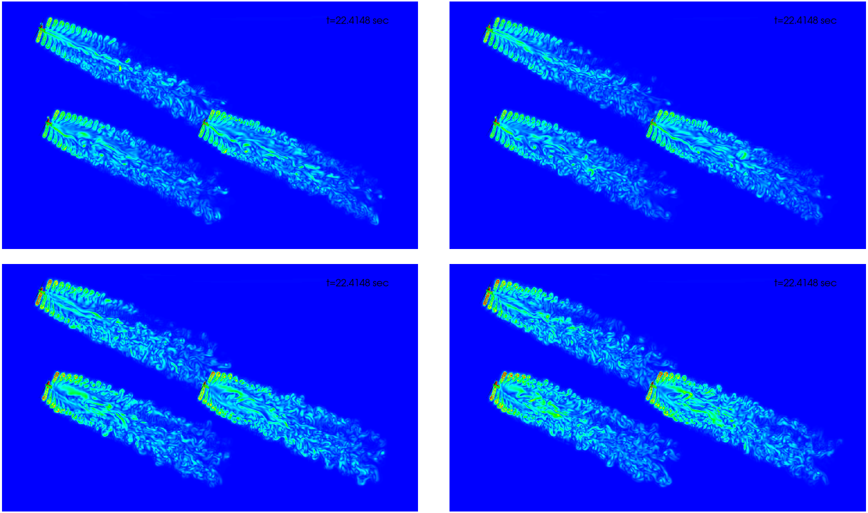

- D3Q27, CSMA with $C_{sm} = 0.14$, WALE with $C_W = 0.5$

Method variation – Wake vorticity field

CSMA WALE

NS

WF

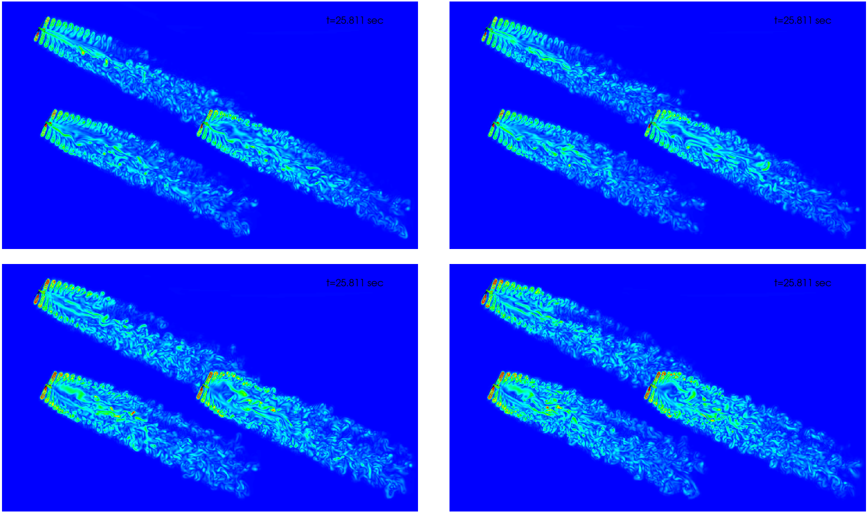

- D3Q27, CSMA with $C_{sm} = 0.14$, WALE with $C_W = 0.5$

Method variation – Wake vorticity field

CSMA WALE

NS

WF

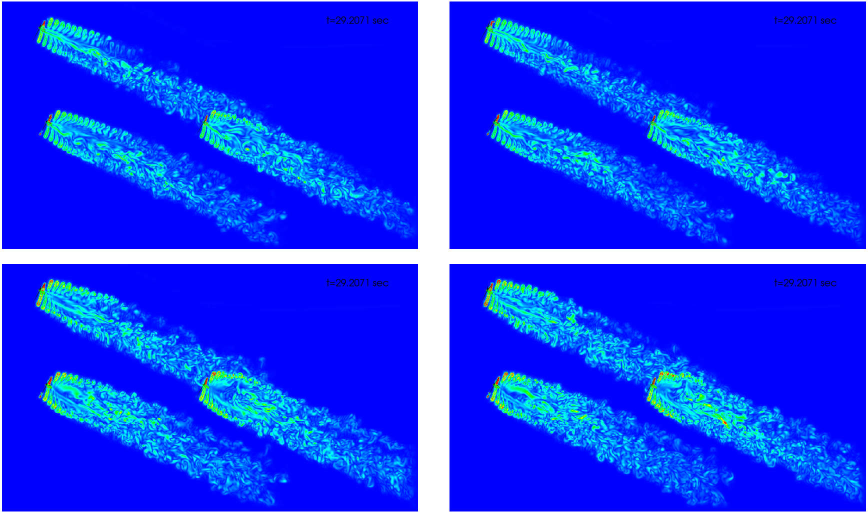

- D3Q27, CSMA with $C_{sm} = 0.14$, WALE with $C_W = 0.5$

Method variation – Wake vorticity field

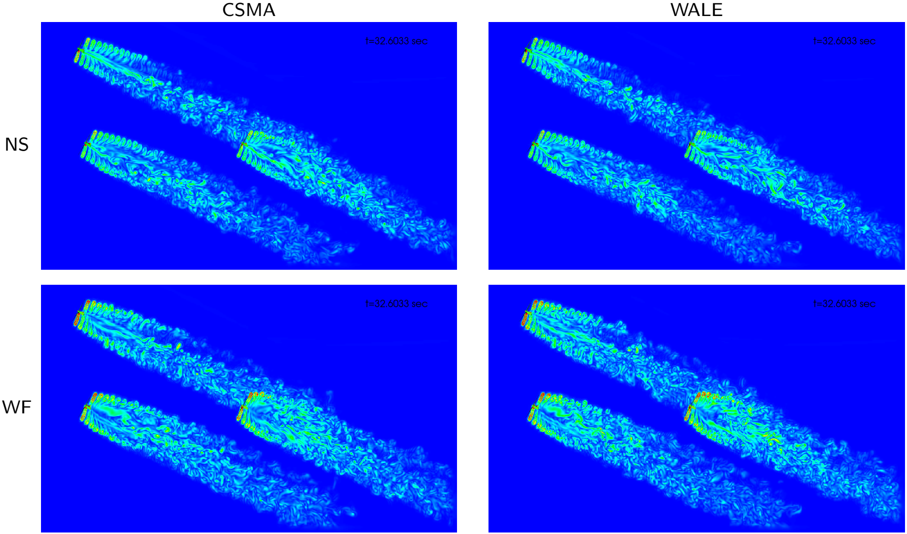

- D3Q27, CSMA with $C_{sm} = 0.14$, WALE with $C_W = 0.5$

Method variation – Wake vorticity field

CSMA WALE

NS

WF

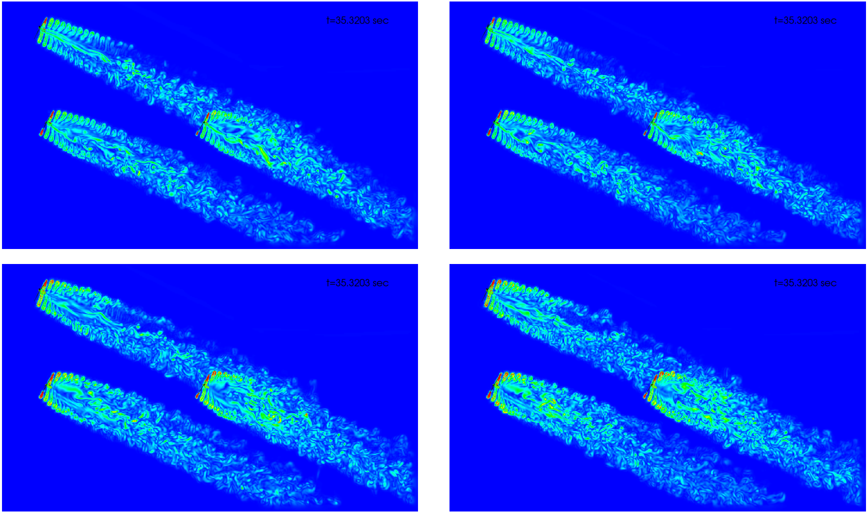

- D3Q27, CSMA with $C_{sm} = 0.14$, WALE with $C_W = 0.5$

Axial velocity, 100-150m downstream, $t = 43\,\mathrm{s}$

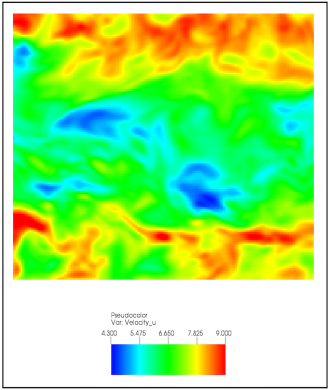

SWIFT

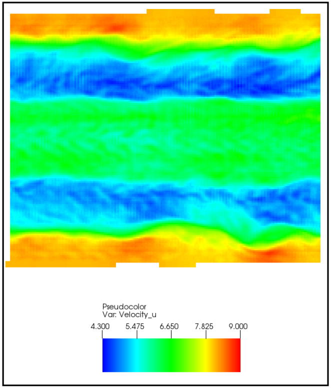

ALM

Vorticity between -5 and 25m downstream, $t = 43\,\mathrm{s}$

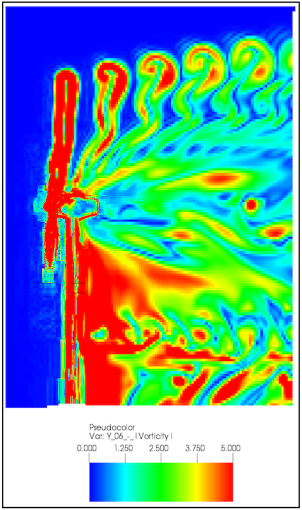

SWIFT

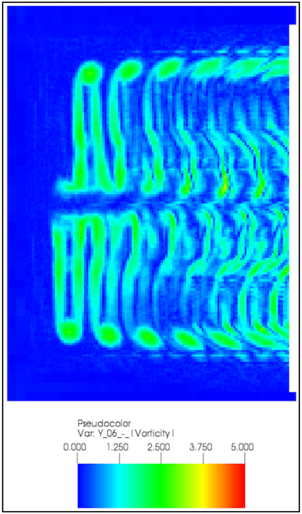

ALM